buildings

Article

Novel Cement-Based Materials Using Seawater, Reused Construction Waste, and Alkali Agents

Yang Bai [1], Yajun Wang [1,2,*], Tao Yang [1] and Xiaoyang Chen [1]

[1] School of Marine Engineering Equipment, Zhejiang Ocean University, Zhoushan 316002, China; baiyang@zjou.edu.cn (Y.B.); yangtao@zjou.edu.cn (T.Y.); chenxiaoyang@zjou.edu.cn (X.C.)
[2] Zhejiang Key Laboratory of Offshore Marine Engineering Technology, Zhoushan 316002, China
* Correspondence: wangyj@zjou.edu.cn

Abstract: This study aimed to develop marine alkali paste (MAP) produced using seawater (SW), recyclable particle material from paste specimens (RPPs), and alkali agents including NaOH (NH) and $Na_2O{\cdot}3SiO_2$ (NS). The physicochemical properties and strength of the MAP were investigated with uniaxial compression tests (UCTs), an Energy-Dispersive Spectrometer (EDS), X-ray diffraction (XRD), and thermal-field emission scanning electron microscopy (SEM). The key information on the MAP preparation and experiments, including mix ratios, ages, curing, and sub-specimen locations, were recorded during the investigation. The results indicated that 8-day-old MAP prepared with NS reached a maximum compressive strength of 8.3 MPa, while 8-day-old NH-prepared specimens achieved up to 5.59 MPa. By 49 days, NS-prepared MAP had strengths between 5.46 MPa and 7.34 MPa, while the strength of NH-prepared MAP ranged from 3.59 MPa to 5.83 MPa. The key hydration products were Friedel's salt ($3CaO{\cdot}Al_2O_3{\cdot}CaCl_2{\cdot}10H_2O$, FS), $x CaO{\cdot}SiO_2{\cdot}nH_2O$ (C-S-H), $CaO{\cdot}Al_2O_3{\cdot}2SiO_2{\cdot}4H_2O$ (C-A-S-H), and $Na_2O{\cdot}Al_2O_3{\cdot}zSiO_2{\cdot}2H_2O$ (N-A-S-H). C-S-H was generated under the critical curing and working conditions in SW. C-A-S-H development contributed to C-S-H network compaction. N-A-S-H development helped in resistance to SO_4^{2-} erosion, thereby cutting down ettringite ($Ca_6Al_2(SO_4)_3(OH)_{12}{\cdot}26H_2O$) development. The active ion exchange between MAP and SW mainly involving SO_4^{2-} and Cl^- led to the significant formation of FS at the interface of C-A-S-H and $x CaO{\cdot}Al_2O_3{\cdot}nH_2O$ (C-A-H). Therefore, FS generation inhibited SO_4^{2-} and Cl^- corrosion in the MAP and rebounded the interface cracks of the hydration products. Consequently, FS contributed to the protection and development of C-S-H in the MAP, which ensured the suitability and applicability of the MAP in marine environments.

Keywords: seawater (SW); reused construction waste (RCW); recyclable particle material from paste specimens (RPPs); alkali agents; marine alkali paste (MAP); strength and physicochemical properties; resource saving

check for updates

Citation: Bai, Y.; Wang, Y.; Yang, T.; Chen, X. Novel Cement-Based Materials Using Seawater, Reused Construction Waste, and Alkali Agents. *Buildings* **2024**, *14*, 3696. https://doi.org/10.3390/buildings14113696

Academic Editor: Grzegorz Ludwik Golewski

Received: 24 October 2024
Revised: 13 November 2024
Accepted: 15 November 2024
Published: 20 November 2024

1. Introduction

Conventional cement-based materials (CCBMs) produced with natural minerals and freshwater (FW) are widely used in global urbanization. The acceleration of global urbanization, which will reach 68% by 2050, means that there is excessive consumption of natural minerals and FW [1]. Also, global urbanization is generating massive amounts of construction waste [2–4]. The ecological environment has been irrecoverably ruined due to the production and application of CCBMs [5,6], as shown in Figure 1.

Reused construction waste (RCW) can partially or completely replace CCBMs, which helps alleviate damage to the ecological environment. RCW contains numerous active silicon and aluminum components that can be activated through thermal [7,8], mechanical [9], and chemical [10,11] methods. The thermal method restores activity, including the rehydration ability and gel formation of RCW, by modifying the composition and structure [7]. Nonetheless, the thermal method introduced involves effectiveness uncertainties for RCW obtained from diverse sources. Additionally, the thermal method consumes a substantial amount of energy, which results in additional carbon emissions. The mechanical method restores the activity of RCW by enhancing its fineness [12–14], which also leads to an additional energy concern. The chemical method restores the activity of RCW by creating an alkali environment or introducing reactive ions [15]. In comparison to the thermal and mechanical ones, the chemical method consumes less energy and exhibits a notable activation effect that depends on the type and content of agents. Zhang [16] examined the effects of mechanical, chemical, and thermal methods on the effective utilization of recycled concrete powder from construction and demolition waste and found that the thermal method at 800 °C was the most effective approach, followed by a chemical approach using a mix of $Ca(OH)_2$ (CH) and $CaSO_4$. Sajedi [17] studied ordinary Portland cement (OPC), as well as slag mortar preparation with three methods, including prolonged grinding, elevated temperature curing, and chemical activation using NaOH and KOH.

Figure 1. Mining and production sites of cement factory in Guangxi province, China.

Excessive FW consumption in CCBM production and application is another concern for the ecological environment in relation to global urbanization. The 2018 edition of the United Nations World Water Development Report stated that by 2050, approximately 6 billion people worldwide will suffer from an FW shortage [18]. In 2050, 75% of FW demand for CCBM production could be sourced from regions that are expected to experience FW stress [19]. Seawater (SW) can partially or completely replace FW used in CCBMs, which helps mitigate the FW shortage issue, particularly in coastal and offshore regions that suffer from substantial availability gaps and the exorbitant transportation expenses of FW. The SW replacement for FW is a growing study interest nowadays [20]. SW can be safely used in CCBMs with suitable measures. Otsuki [21] proposed and demonstrated the possibility of using SW in concrete. Sheng [22] used SW and sea sand in the production of mortar and showed improved performance in the marine environment. The improvement was attributed to the anion–cation exchange between the paste and sea sand, the polymerization effect of Friedel's salt ($3CaO{\cdot}Al_2O_3{\cdot}CaCl_2{\cdot}10H_2O$, FS), and the continuous hydrate development with age accumulation. Shi [23] used a chemical method to produce alkali-activated materials that were mixed with SW and FW, and the results showed that SW treatment also generated advantageous products, the main contents of which included the amorphous gels of C-(A)-S-H, M-S-H, and SiO_2.

SW and RCW treated with chemical methods can be adopted for novel CBM (NCBM) production in marine environments, where natural mineral and FW shortages give rise to concerns about the ecological environment and CCBM applicability. The NCBM produced with SW and RCW also shows merits including economy, recyclability, applicability, and lower carbon emissions. The successful application of the NCBM produced with SW and RCW necessarily resorts to proper treatment on complicated ions including Cl^-, Na^+, SO_4^{2-}, CO_3^{2-}, etc. The precise quantification on the physicochemical properties of RCW and its products helps properly treat the complicated ions. Therefore, this study developed the simulated RCW and its products. Meanwhile, this study provided the precise physicochemical properties of all the involved materials in addition to their process in detail including mix ratio, preparation, and curing, which played a key role in the successful application of the NCBM produced with SW and RCW.

The simulated RCW in this study contained all the parental specimens (PSs) that were produced with a certain process in the laboratory where the key conditions, including time, temperature, relative humidity (RH), etc., were exactly operated. The simulated RCW products consist of the recyclable particle material from paste specimens (RPPs) and marine alkali paste (MAP). PSs were made of OPC and FW at a designed mix ratio, which simulated construction. Subsequently, PSs were subjected to uniaxial compression tests (UCTs), and the broken specimens were collected. This process simulated demolition. The broken specimens were then treated with mechanical methods including bistage crushing and screening to obtain RPPs. Finally, MAP was produced using SW, RPPs, and alkali agents including NH and NS with the designed mix and then cured in SW. The physicochemical properties and strength of PSs, RPPs, and MAP were investigated using UCTs, an Energy-Dispersive Spectrometer (EDS), X-ray diffraction (XRD), and thermal-field emission scanning electron microscopy (SEM). The relation between the physicochemical properties and strength of the simulated RCW and its products developed in this study was also explored.

2. Materials and Methods

2.1. Materials

The PSs in this study were produced for RPP creation at the Zhejiang Key Laboratory of Marine Engineering Technology (Zhoushan, China). The production, curing, demolding, and UCTs of PSs referred to Sino standards GB/T 1346-2011 [24] and GB/T 17671-2021 [25] to accurately simulate the construction materials employed in situ. The PSs' designed mix ratio was FW/cement = 1:0.458. This study employed iron molds with dimensions of 70.7 mm × 70.7 mm × 70.7 mm for PS pouring. The PSs underwent curing with the precise control on time, temperature, and RH for 40 days that included the following: 24 h in the laboratory under a temperature of 20 ± 2 °C and RH of 60% and following 39 days in a standard curing room under a temperature of 20 ± 1 °C and RH of 90%. UCTs were then performed for the PSs. The specimens were treated with bistage crushing and screening that were the crucial process in the mechanical method once UCTs ended. The bistage crushing was composed of rough and fine ones. The rough crushing was performed using a CY-12 hammer crusher (Shicheng Jinchuan Mineral Equipment Manufacturing Co., Ltd., Shicheng, China) which had a capacity of 0.0016 m^3 per cycle for 1 min. The rough crushing reduced the specimens' size below 5 mm. The products from the CY-12 hammer crusher then underwent fine crushing using a QE-500 portable fine crusher (Zhejiang Harry Industrial & Trade Co., Ltd., Jinhua, China). After fine crushing, the specimens were screened with a 0.075 mm stainless steel sieve to obtain RPPs. The RPPs were then mixed with NH and SW or NS and SW to produce MAP.

The information on the materials used in this study is provided in detail as follows.

FW: FW for PS production was sourced from Changzhi Island, China. The key ions in the FW included Cl^- at 80.97 ppm (mg/kg), Na^+ at 59.50 ppm, SO_4^{2-} at 37.76 ppm, Ca^{2+} at 29.30 ppm, K^+ at 9.85 ppm, and Mg^{2+} at 6.95 ppm.

SW: SW for MAP production was sourced from Changzhi Island Wharf, China. The key ions in the SW included Cl^- at 17,552.13 ppm, Na^+ at 8704.95 ppm, SO_4^{2-} at 2650.55 ppm, Mg^{2+} at 962.49 ppm, K^+ at 466.41 ppm, and Ca^{2+} at 6.95 ppm.

NH: NH with a density of 2.13 g/cm^3 and concentration of 10.83 mol/L was manufactured by Shanghai Zhan Yun Chemical Co., Ltd. (Shanghai, China).

NS: NS with a density of 1.36 g/cm^3, modulus of 3.3, and concentration of 60 g/L was manufactured by Shandong Yousu Chemical Technology Co., Ltd. (Weifang, China).

Cement: The P.O.42.5 cement was manufactured by Ningbo Hailuo Cement Co., Ltd. (Ningbo, China). The cement composition was analyzed using an EDS (EDAX Inc., Mahwah, NJ, USA); XRD (BRUKER AXS Inc., Madison, WI, USA); and SEM (TESCAN ORSAY HOLDING, a.s., Brno, Czech Republic). The main components of the cement include $3CaO{\cdot}SiO_2$ (C_3S), $2CaO{\cdot}SiO_2$ (C_2S), $4CaO{\cdot}Al_2O_3{\cdot}Fe_2O_3$ (C_4AF), $3CaO{\cdot}Al_2O_3$ (C_3A), $CaSO_4{\cdot}2H_2O$, Al_2O_3, SiO_2, CaO, and $CaMg(CO_3)_2$, as shown in Figure 2.

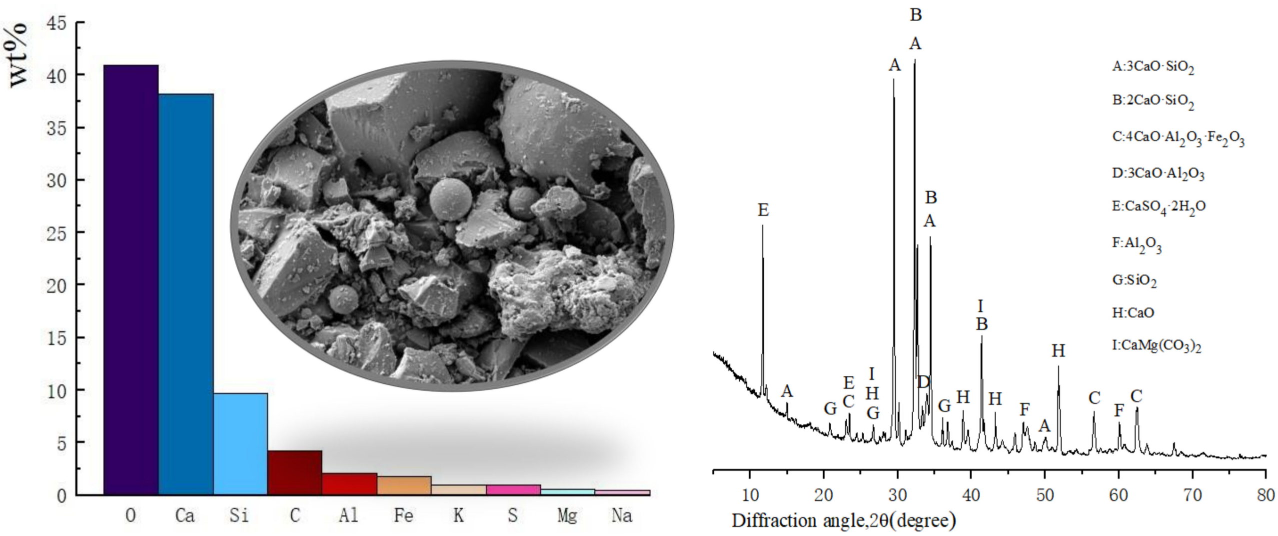

(**a**) (**b**)

Figure 2. Cement composition. (**a**) Element content; (**b**) XRD patterns.

2.2. Methods

2.2.1. PS Production

In total, 30 PSs with the designed mix ratio FW/cement =1:0.458 were produced based on the Sino standard GB/T 1346-2011 [24] using a JJ-5 mixer (Hebei Dahong Laboratory Instrument Co., Ltd., Cangzhou, China) with a power of 1.6 kW. The properly mixed paste was poured into 70.7 mm × 70.7 mm × 70.7 mm iron molds and compacted using a ZDS0101 vibration table for 10 min. The vibration frequency and amplitude of ZDS0101 (Henan Shuangmu Machinery Manufacturing Co., Ltd., Xinxiang, China) were 45 HZ and 0.3 mm, respectively. The PSs were then initially cured and demolded indoors for 1 day at a controlled temperature of 20 ± 2 °C and RH of 60%. This was achieved through the use of an air conditioning system and a dehumidifier, both set to the specified parameters to ensure stable and controlled conditions within the enclosed space. The demolded PSs were transferred to a standard curing room under a temperature of 20 ± 1 °C and RH of 90% for the 39 days of standard curing. These conditions were regulated using built-in instruments that allow precise control over temperature and humidity, ensuring consistent curing conditions for all specimens. The flowchart of PS production is shown in Figure 3. The PS strength was evaluated under the loading rate 5 kN/s by a YAW-2000 machine, the parameters of which are shown in Table 1. The expected strength of the PSs was 58 MPa.

Table 1. Uniaxial compression system parameters.

Maximal Stroke of Vertical Main Shaft (mm)	Minimal Load Rate (kN/s)	Maximal Load Rate (kN/s)	Extreme Load (kN)	Power (kW)	Platform Area (mm^2)
260	0.5	30	300	0.75	1.47×10^4

Figure 3. Flowchart of PS production.

2.2.2. RPP Production

The bistage crushing in this study for RPP production was conducted using a CY-12 hammer and QE-500 portable crusher. The destructed PSs in UCTs were roughly crushed at first with a CY-12 hammer, the key parameters of which included an external size of 1170 mm × 720 mm × 1090 mm, a maximum internal capacity of 0.06 m^3, power of 7.5 kW, and a rotation speed of 14,000 r/min. The size of the products from the CY-12 hammer was below 5 mm. The products were then finely treated with a QE-500 portable crusher, the key parameters of which included an external size of 140 mm × 140 mm × 330 mm, a maximum internal capacity of 570.2 cm^3, power of 1.6 kW, and a rotation speed of 28,000 r/min. The products from the QE-500 portable crusher were screened with the 0.075 mm stainless steel sieve, and the screened particle materials, the size of which was below 0.075 mm, were RPPs that had achieved the optimal physical activity [26]. The flowchart of RPP production is shown in Figure 4.

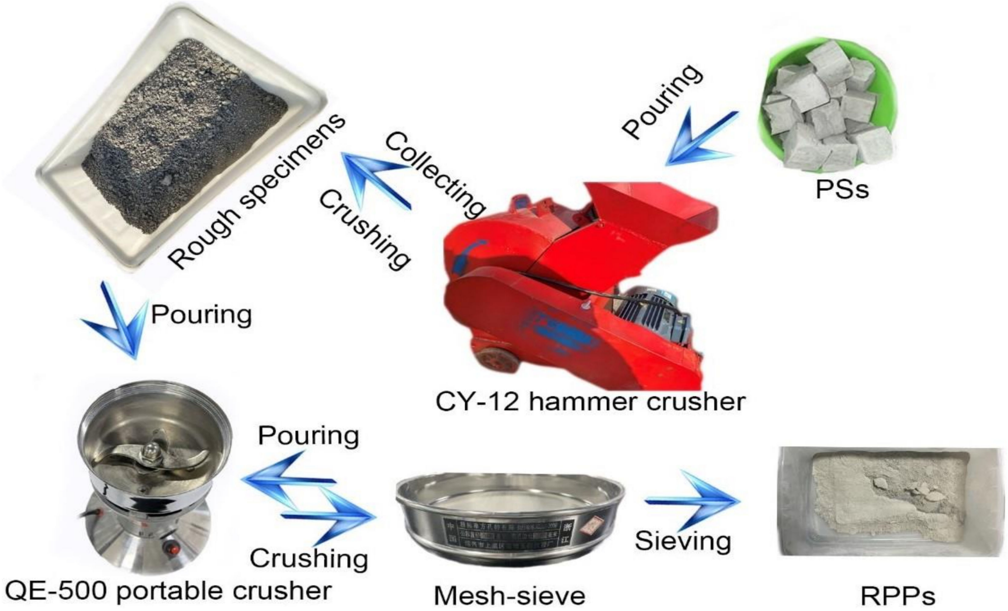

Figure 4. Flowchart of PS production.

2.2.3. MAP Production

The alkali activation using SW, RPPs, and alkali agents was adopted for MAP production. The mix ratios in Table 2 were developed at the School of Marine Engineering Equipment, Zhejiang Ocean University (Zhoushan, China). MAP was prepared using NH and NS, respectively. Hence, this study developed 7 mix ratios that included 4 NH programs and 3 NS ones. The MAP mix ratios in Table 2 were expressed based on the mass ratios of the compositions. The compositions including SW, RPPs, NH, and NS were weighed according to Table 2 with an accuracy of ±0.01 g.

Table 2. MAP production programs.

Mix Ratio Codes	Mix Ratio Expressions (kg)	Age (Days)	Specimen Codes	Testing Zone	Sub-Specimen Codes
MAP1	RPP:NH:SW= 1.6:0.288:0.672	8	MAP1-8	BZ	MAP1-8-BZ
				nBZ	MAP1-8-nBZ
		49	MAP1-49	BZ	MAP1-49-BZ
				nBZ	MAP1-49-nBZ
MAP2	RPP:NH:SW= 1.6:0.288:0.768	8	MAP2-8	BZ	MAP2-8-BZ
				nBZ	MAP2-8-nBZ
		49	MAP2-49	BZ	MAP2-49-BZ
				nBZ	MAP2-49-nBZ
MAP3	RPP:NH:SW= 1.6:0.192:0.768	8	MAP3-8	BZ	MAP3-8-BZ
				nBZ	MAP3-8-nBZ
		49	MAP3-49	BZ	MAP3-49-BZ
				nBZ	MAP3-49-nBZ
MAP4	RPP:NH:SW= 1.6:0.096:0.768	8	MAP4-8	BZ	MAP4-8-BZ
				nBZ	MAP4-8-nBZ
		49	MAP4-49	BZ	MAP4-49-BZ
				nBZ	MAP4-49-nBZ
MAP5	RPP:NS:SW= 1.6:0.288:0.768	8	MAP5-8	BZ	MAP5-8-BZ
				nBZ	MAP5-8-nBZ
		49	MAP5-49	BZ	MAP5-49-BZ
				nBZ	MAP5-49-nBZ
MAP6	RPP:NS:SW= 1.6:0.192:0.768	8	MAP6-8	BZ	MAP6-8-BZ
				nBZ	MAP6-8-nBZ
		49	MAP6-49	BZ	MAP6-49-BZ
				nBZ	MAP6-49-nBZ
MAP7	RPP:NS:SW= 1.6:0.096:0.768	8	MAP7-8	BZ	MAP7-8-BZ
				nBZ	MAP7-8-nBZ
		49	MAP7-49	BZ	MAP7-49-BZ
				nBZ	MAP7-49-nBZ

Figure 5 shows the MAP production process. NH and NS were diluted with SW in the 300 mL beaker to be the mixing solution. RPPs were then poured into the JJ-5 mixing tank and formed the inverted cone shape. The mixing solution was injected into the center of the inverted cone. The mixture of RPPs and mixing solution was stirred in the JJ-5 mixing tank at a low speed of 1.5 r/s for 120 s, allowed to rest for 60 s, and then stirred at a high speed of 3.0 r/s for another 120 s. The prepared paste was defined as MAP. MAP was filled in the 70.7 mm × 70.7 mm × 70.7 mm iron molds and compacted using a ZDS0101 vibration table for 10 min. The compacted MAP was left indoors at a controlled temperature of 20 ± 2 °C and RH of 60% for 24 h to develop initial strength. The MAP was then demolded and transferred to the standard curing room under a temperature of 20 ± 1 °C and RH of 90%. Furthermore, the MAP specimens in the standard curing room were completely submerged in SW tanks to simulate a marine environment. The MAP ages in this study were 8 and 49 days.

Figure 5. Flowchart of MAP production.

The comprehensive experiments including UCTs, an EDS, SEM, and XRD were invited to evaluate the performance of MAP. The sub-specimens investigated with an EDS, SEM, and XRD in this study were taken from the fracture zones and intact fragments of the MAP specimens that had been destructed in UCTs, respectively. Therefore, the locations of the broken zones and intact ones where the sub-specimens were taken from were defined correspondingly as BZs and nBZs.

3. Results and Analysis

The strength performance of 14 MAP specimens and the physicochemical properties of 28 sub-specimens were investigated in this study based on UCTs, an EDS, SEM, and XRD results that incorporated key information including mix ratios, ages, curing, and sub-specimen locations.

3.1. Date Analysis of RPPs

3.1.1. EDS Results of RPPs

EDS results indicated that O, Ca, and C were the leading elements in RPPs, as shown in Figure 6.

C Wt% in RPPs increased by 10.11% in comparison with that in P.O.42.5 cement. RPPs achieved significant physical activity by virtue of the bistage crushing that also generated a larger specific surface area in the particle materials, which intensified the carbonization and increased C Wt% in RPPs.

In terms of Ca and Si in RPPs, the Wt% retention percentages were 90.11% and 49.43% in comparison with those in P.O.42.5 cement, which were advantageous for the MAP performance. There was a significant presence of Ca and Si with the formation of C-S-H, a primary strength-giving phase in MAP. Higher Ca and Si Wt% retention percentages correspond to the densification of the C-S-H and C-A-S-H gels, which contribute to the material's mechanical properties and durability. Meanwhile, Na was eliminated during RPP production. Na elimination resulted from the reaction of Na_2O in cement, H_2O and

CO_2 in the air, and $Na_2CO_3{\cdot}10H_2O$ development. $Na_2CO_3{\cdot}10H_2O$ easily disappeared due to weathering. The process is expressed in Equations (1)–(3) as follows:

$$Na_2O + H_2O = 2NaOH \tag{1}$$

$$2NaOH + CO_2 = Na_2CO_3 + H_2O \tag{2}$$

$$Na_2CO_3 + 10H_2O = Na_2CO_3{\cdot}10H_2O \tag{3}$$

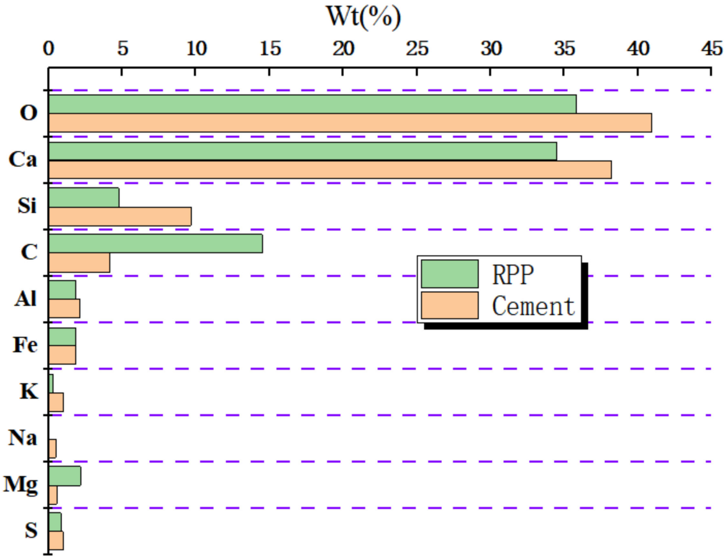

Figure 6. EDS results of RPPs and cement.

3.1.2. XRD Results of RPPs

The RPP XRD pattern reported new product generation including $CaCO_3$, $Fe(OH)_3$, $Ca_6Al_2(SO_4)_3(OH)_{12}{\cdot}26H_2O$ (Al-Ettringite), $Ca_3(Al_{0.8}Fe_{0.2}){\cdot}3CaSO_4{\cdot}32H_2O$ (Fe-Ettringite), CH, xCaO·$SiO_2{\cdot}n H_2O$ (C-S-H), xCaO·$Al_2O_3{\cdot}nH_2O$ (C-A-H), and $CaO{\cdot}Al_2O_3{\cdot}2SiO_2{\cdot}4H_2O$ (C-A-S-H), as shown in Figure 7. Particularly, two ettringites developed in RPPs including Al-Ettringite and Fe-Ettringite that were formed through the hydration process of C_3A and C_4AF in the presence of gypsum.

The ettringite crystal belonged to the trigonal crystal system, with a space group of P31c and unit cell parameter of a = b=1.126 nm and c = 2.148 nm [27].

$\{Ca_6[Al(OH)_6]_2{\cdot}24H_2O\}^{6+}$ was the fundamental structural unit of the ettringite and was composed of octahedra $[Al(OH)_6]^{3-}$ and polyhedra CaO_8.

The cylinder $[Ca_3Al(OH)_6{\cdot}12H_2O]^{3+}$ served as the basis of the ettringite with $SO_4{}^{2-}$ ions and gap H_2O that were arranged in a hexagonal pattern around the axis [28,29]. Al^{3+} in ettringite could be substituted by Fe^{3+}, Cr^{3+}, and Mn^{3+}. Ca^{2+} in ettringite could be replaced by Zn^{2+}, Mg^{2+}, Co^{2+}, Ni^{2+}, Mn^{2+}, and Fe^{2+}. $SO_4{}^{2-}$ in ettringite could be partially or completely substituted by $CO_3{}^{2-}$, $NO_3{}^{2-}$, $SeO_4{}^{2-}$, $CrO_4{}^{2-}$, and $B(OH)_4{}^{-}$. Particularly, the partial substitution of Fe^{3+} for Al^{3+} in Al-Ettringite resulted in the formation of Fe-Ettringite.

Therefore, the development of Al-Ettringite and Fe-Ettringite in RPPs is expressed in Equations (4) and (5) as follows:

$$C_3A + 3CaSO_4{\cdot}2H_2O + 26H_2O \rightarrow Ca_6Al_2(SO_4)_3(OH)_{12}{\cdot}26H_2O \tag{4}$$

$$4C_4AF + 15CaSO_4{\cdot}2H_2O + 140H_2O \rightarrow 5[Ca_3(Al_{0.8}Fe_{0.2}){\cdot}3CaSO_4{\cdot}32H_2O] + 6Fe(OH)_3 + Ca(OH)_2 \tag{5}$$

Moreover, the RPP XRD pattern indicated that C_4AF was consumed during ettringite development.

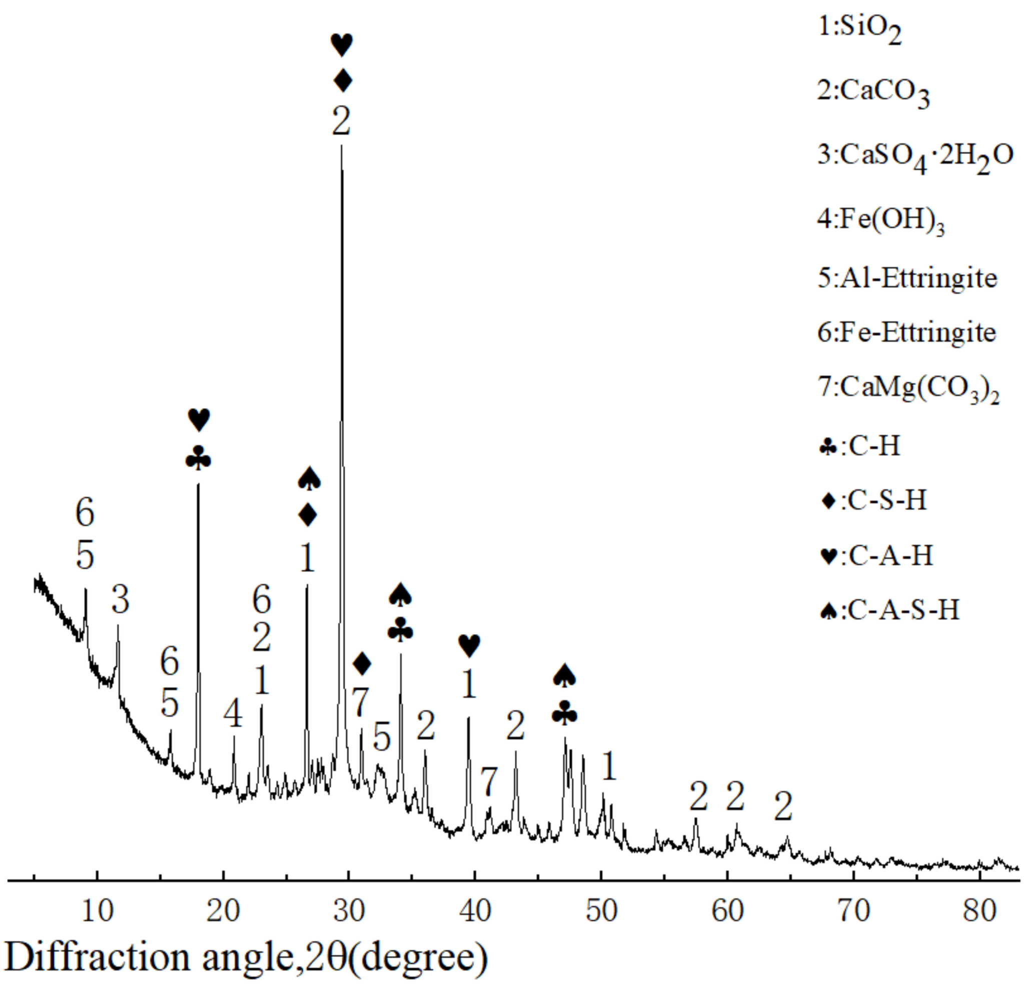

Figure 7. RPP XRD pattern.

3.2. Date Analysis of MAP

3.2.1. UCT Results of MAP

This study computed MAP strength by Equation (6) as follows:

$$\sigma = \frac{W_u}{A_0} \tag{6}$$

where W_u represented the maximum load of the UCTs, and A_0 = 70.7 × 70.7 mm^2 denoted the cross-sectional area of the MAP specimen. Based on Equation (1), Figure 8 illustrates the strength distribution of 14 MAP specimens in Table 2.

MAP specimens MAP2-8 and MAP2-49 cured in SW disintegrated at 3 days old and reported no strength values, as shown in Figure 8.

The MAP specimens produced with NH at 8 days old achieved the maximal strength 5.59 MPa (MAP4-8) and the minimal strength 3.98 MPa (MAP1-8). The maximal and minimal strengths of the MAP specimens produced with NS at 8 days old were 8.3 MPa (MAP5-8) and 6.18 MPa (MAP7-8), respectively.

The expected strengths for the MAP specimens produced with NH and NS at 8 days old were correspondingly 4.65 MPa and 7.27 MPa. Therefore, the overall expected strength for all MAP specimens at 8 days old was 5.96 MPa.

The lowest strength for the MAP specimens at 8 days old produced with NS was 9.54% higher than the highest strength of that produced with NH.

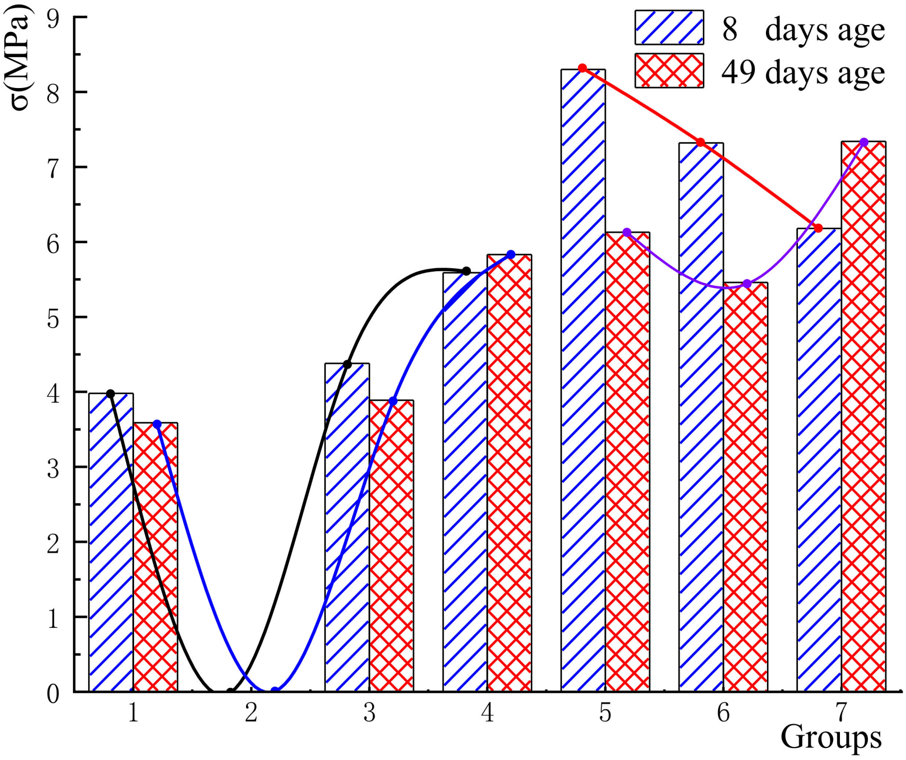

Figure 8. MAP strength distribution.

The maximal and minimal strengths of the MAP specimens produced with NH at 49 days old reached 5.83 MPa (MAP4-49) and 3.59 MPa (MAP1-49), respectively. By contrast, the maximal and minimal strengths of the MAP specimens produced with NS at 49 days old were 7.34 MPa (MAP7-49) and 5.46 MPa (MAP6-49), respectively.

The expected strength for the MAP specimens produced with NH at 49 days old was 4.44 MPa, which indicated a 4.52% decrease in comparison with those at 8 days old. Meanwhile, the expected strength for the MAP specimens produced with NS at 49 days old was 6.31 MPa, which showed a 13.2% decrease in comparison with those at 8 days old. Hence, the overall expected strength for all MAP specimens at 49 days old was 5.37 MPa, which revealed a 9.9% decrease in comparison with those at 8 days old. There was a difference, however, in the MAP specimens prepared with the mix ratios MAP4 and MAP7 by which their strengths presented 4.12% and 15.8% rises with ages from 8 days to 49 days.

3.2.2. EDS Results of MAP

The EDS results of 28 sub-specimens are summarized in Figure 9. The main elements included Ca, Si, C, Fe, Al, Na, Cl, Mg, and S, which determined the strength and physicochemical behavior of the MAP.

Ca Wt% in all the MAP specimens was above 20%. The Ca^{2+} supply developed abundantly in MAP and could help generate complete Ca^{2+} complexes including C-A-H, C-S-H, and C-A-S-H. The Ca content in MAP produced with NS at 49 days old increased with the NS concentration decrease. The Si content in sub-specimens from BZs produced with NH at 8 days old decreased with the NH concentration increase. The Si content in sub-specimens from nBZs produced with NS at 49 days old increased with the NS content increase. The C content in sub-specimens from BZs produced with NH at 49 days old decreased with the NH concentration increase. The Cl content in sub-specimens from nBZs produced with NH at 8 days old decreased with the NH concentration increase. The Cl content in sub-specimens from BZs produced with NS at 49 days old decreased with the NS concentration increase.

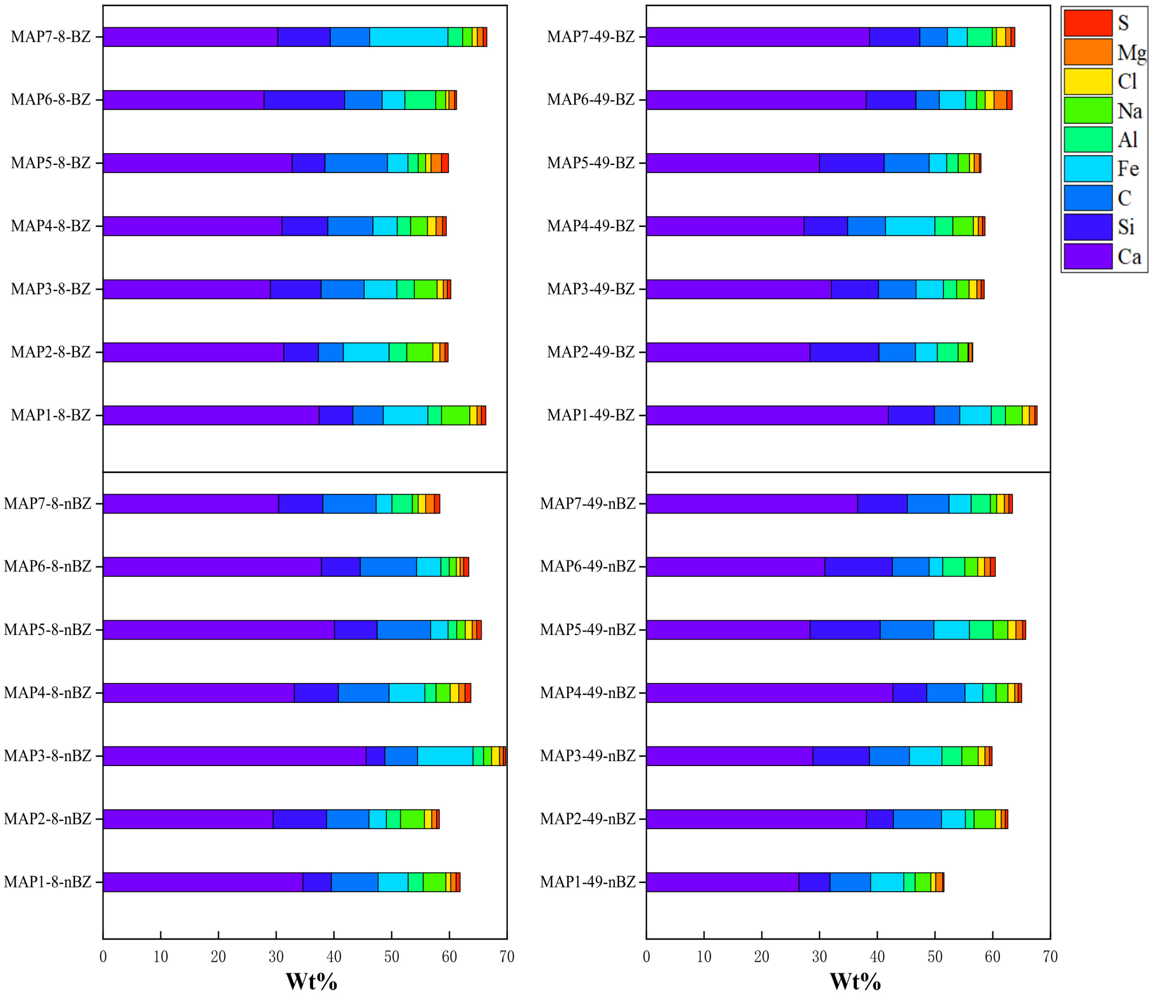

Figure 9. The elemental content of each group of MAP.

3.2.3. XRD Results of MAP

1. XRD Analysis of MAP: NH as Alkali Agent

The main peak heights in XRD patterns of the sub-specimens from BZs at 8 and 49 days old ascended with the NH concentration increase, as shown in Figure 10.

The XRD results indicated that in MAP production there was the NH critical concentration (CC) beyond which MAP hydration was suppressed. Hence, a polynomial regression model was established in this study to predict the CC based on the XRD results and NH concentration. The polynomial regression model is expressed in Equation (7).

$$y = -19379 + 326213.54x - 784233.94x^2 \tag{7}$$

The polynomial regression model is described in Figure 11 according to which the NH CC was 0.208.

The excessive NH concentration that exceeded the CC brought about the higher solubility of OH^- ions, which caused the rapid formation of the hydrates that showed the film-like feature. The film-like hydrates were developed on the RPP surface and prevented further alkali activation reaction with its thickness growth. Therefore, both the main peak heights in XRD patterns where hydrates including C-S-H, $Na_2O{\cdot}Al_2O_3{\cdot}xSiO_2{\cdot}2H_2O$ (N-A-S-H), C-A-S-H, and ettringite were present and the strength of the MAP specimens decreased. The MAP specimens produced with excessive NH concentration that exceeded the CC included MAP1-8, MAP1-49, MAP3-8, and MAP3-49.

The NH preparation generated several new hydrates in MAP such as N-A-S-H, FS, $3CaO \cdot Al_2O_3 \cdot CaSO_4 \cdot 12H_2O$ (monosulfate), $4CaO \cdot Al_2O_3 \cdot 13H_2O$ (C_4AH_{13}), $3CaO \cdot Al_2O_3 \cdot CaCO_3 \cdot 32H_2O$ (CO_3-Ettringite), and $Mg_6Al_2CO_3(OH)_{16} \cdot 4H_2O$ (Hydrotalcite), as shown in Figure 10.

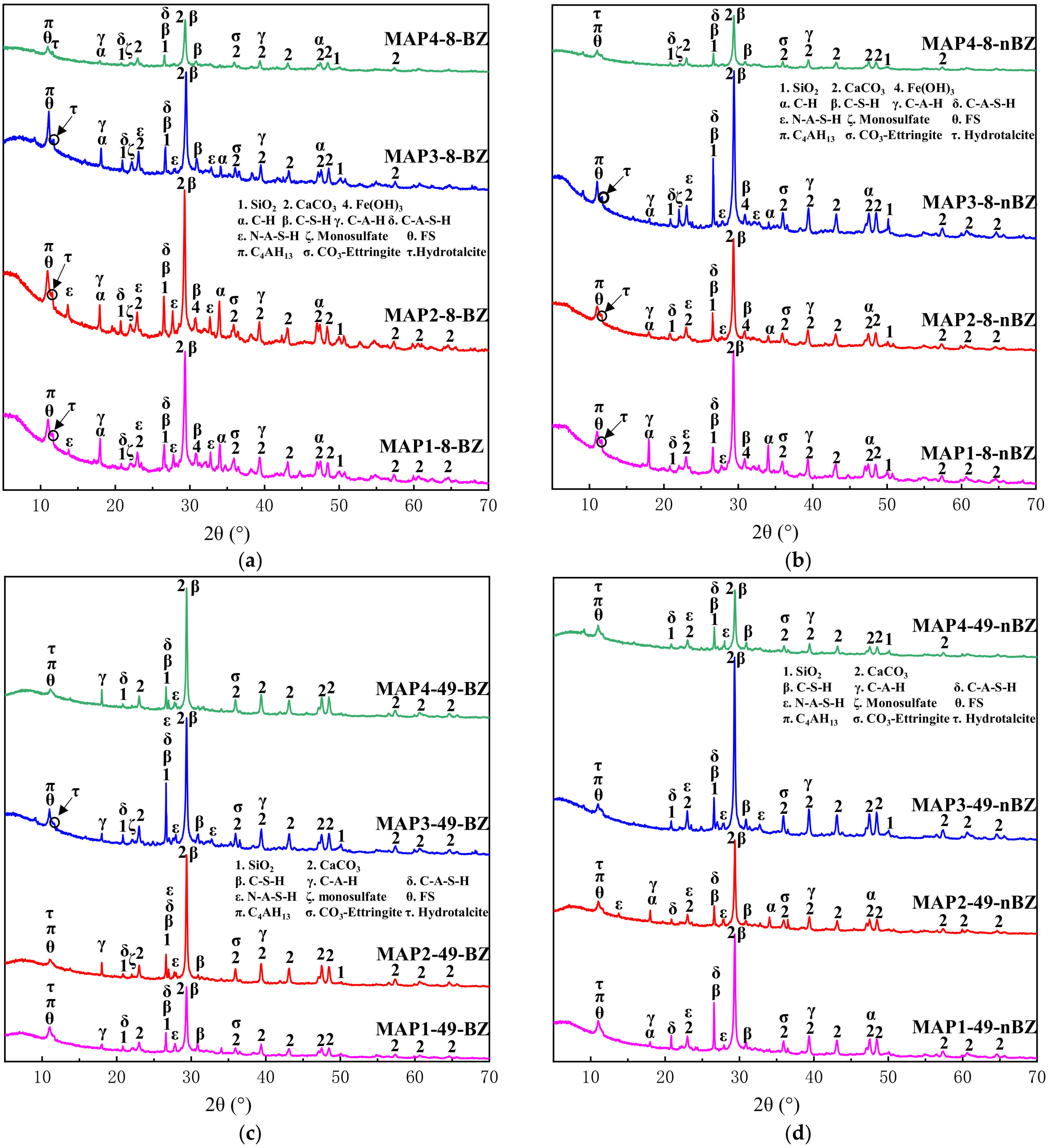

(**a**) (**b**) (**c**) (**d**)

Figure 10. XRD patterns of NH as alkali agent. (**a**) XRD patterns at the BZ position for 8 days old; (**b**) XRD patterns at the nBZ position for 8 days old; (**c**) XRD patterns at the BZ position for 49 days old; (**d**) XRD patterns at the nBZ position for 49 days old.

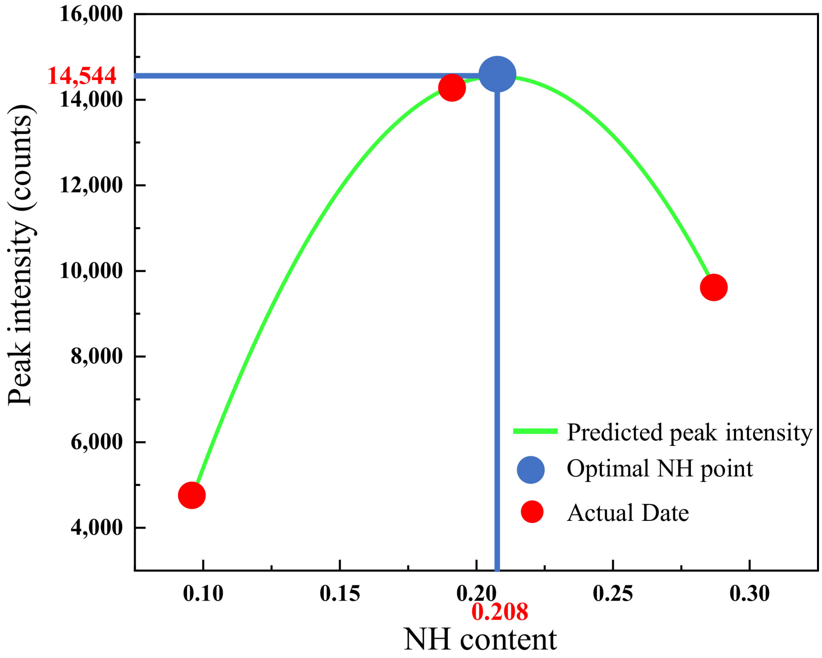

Figure 11. NH CC polynomial regression prediction model.

N-A-S-H gel with the three-dimensional network formed by $[SiO_4]^{4-}$ and $[AlO_4]^{5-}$ tetrahedra exhibits good resistance to corrosive environment ions [30–32]. Particularly, there was a certain relation between N-A-S-H development and NH concentration, as shown in Figure 12. The mix ratio MAP4 reported the lowest NH concentration. Therefore, the MAP specimens prepared with MAP4 accommodated a lower OH^- concentration that failed to sufficiently dissolve $[SiO_4]^{4-}$ and $[AlO_4]^{5-}$, which resulted in the limited N-A-S-H formation. By contrast, more N-A-S-H gel was developed in the MAP specimens produced with the mix ratio MAP3. The NH concentration of the mix ratio MAP3 was the closest one to the NH CC, which offered the advantageous hydration for $[SiO_4]^{4-}$ and $[AlO_4]^{5-}$.

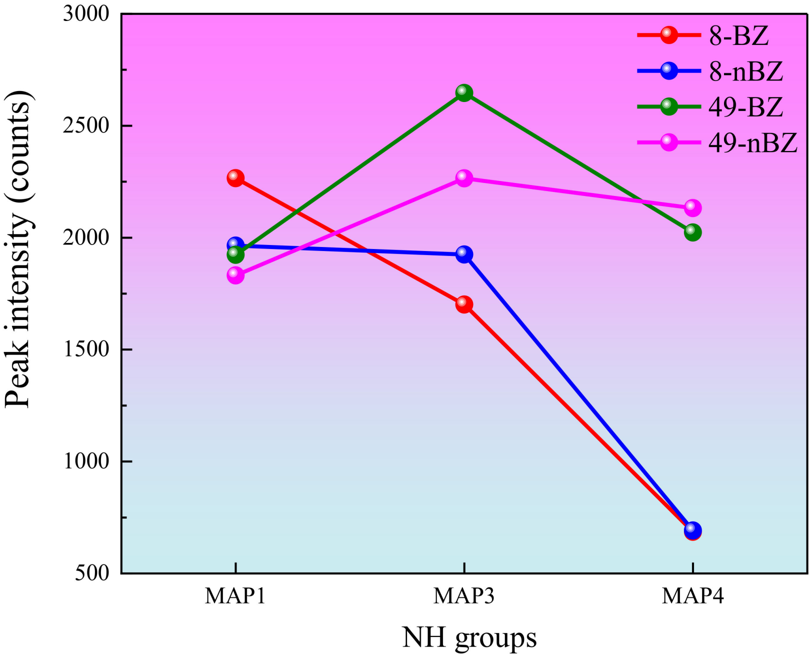

Figure 12. The main peak diffraction peak intensity of N-A-S-H under each ratio of NH groups (the content of MAP1 and MAP2 NH was the same and the MAP2 group collapsed, with this not included in the discussion here).

In terms of the sub-specimens from BZs and nBZs at 8 days old, the heights of the peaks where N-A-S-H was present ascended with NH concentration increase, as shown in Figure 12. The NH concentration on the margin of the CC affected N-A-S-H development in the grown MAP. A lower NH concentration caused hydration to stop; an excessive NH concentration led to the rapid accumulation of the film-like hydrates on the RPP surface, which also hindered further hydration and N-A-S-H development.

XRD results revealed the presence of monosulfate that was transformed from ettringite, as shown in Figure 10. Meanwhile, the N-A-S-H gel helped establish the consistent framework in MAP that achieved resistance against SO_4^{2-} intrusion, which cut down ettringite development. Furthermore, N-A-S-H and ettringite also competed for aluminate. Eventually, monosulfate was transformed from ettringite (Equation (8)). Simultaneously, anions including Cl^- and CO_3^{2-} were significantly generated in MAP and adsorbed frequently by the matrix of MAP due to chemisorption. Hence, $[Ca_2Al(OH)_6]^+$ in monosulfate and Cl^- generated prior to chemisorption and a more stable FS structure were created due to the abundant supplementation of $[Ca_2Al(OH)_6]^+$ and Cl^- complexes in MAP (Equation (9)). Furthermore, chemisorption inhibited Cl^- corrosion in MAP. The ettringite was also partially eroded by CO_3^{2-}, which resulted in CO_3-Ettringite generation (Equation (10)).

$$2(3CaO\cdot Al_2O_3) + 3CaO\cdot Al_2O_3\cdot CaSO_4\cdot 32H_2O + 4H_2O \rightarrow 3(3CaO\cdot Al_2O_3\cdot CaSO_4\cdot 12H_2O) \tag{8}$$

$$3CaO\cdot Al_2O_3\cdot CaSO_4\cdot 10H_2O + 2Cl^- \rightarrow 3CaO\cdot Al_2O_3\cdot CaCl_2\cdot 10H_2O + SO_4^{2-} + 2H_2O \tag{9}$$

$$3CaO\cdot Al_2O_3\cdot 3CaSO_4\cdot 32H_2O + 3CO_3^{2-} \rightarrow CaO\cdot Al_2O_3\cdot 3CaCO_3\cdot 12H_2O + 3SO_4^{2-} \tag{10}$$

2. XRD analysis of MAP: NS as alkali agent

The main peak heights in XRD patterns of the sub-specimens from both BZs and nBZs at 8 and 49 days old ascended with the NS concentration increase, as shown in Figure 13.

The NS preparation provided abundant OH^- and $[SiO_4]^{4-}$ in MAP. The OH^- supply promoted the matrix depolycondensation that released Ca^{2+} and Al^{3+} and facilitated the =Si-O-Si= and ≡Al-O-Al≡ bond cleavage. The repolycondensation of $[SiO_4]^{4-}$ and $[AlO_4]^{5-}$ then took place in the OH^- environment where the $[SiO_4]^{4-}$ concentration increased. Therefore, the reaction of $[SiO_4]^{4-}$, $[AlO_4]^{5-}$, and Ca^{2+} was intensified and C-S-H, C-A-H, and C-A-S-H developed efficiently in MAP.

The heights of the peaks where C-S-H, C-A-H, and C-A-S-H were detected in BZs and nBZs of the sub-specimens at 8 days old rose with the NS concentration increase. Especially, the heights of the main peaks where C-S-H was present ascended with the NS concentration increase in the sub-specimens at 8 days old, with the strength of MAP also being reported with this rising behavior. Furthermore, the heights of the main peaks where C-S-H was present in the nBZs were higher than those in the BZs.

Monosulfate, FS, CO_3-Ettringite, and hydrotalcite were formed in the BZs of the sub-specimens prepared with NS at 8 days old. Meanwhile, FS and hydrotalcite were generated in the nBZs of the sub-specimens prepared with NS at 8 days old. CO_3-Monosulfate was observed in the BZ of the sub-specimen prepared with NS at 49 days old, as shown in Figure 13.

The heights of the peaks where C-S-H, C-A-H, and C-A-S-H were detected in BZs and nBZs of the sub-specimens at 8 days old rose with the NS concentration increase. Especially, the heights of the main peaks where C-S-H was present ascended with the NS concentration increase in the sub-specimens at 8 days old, with the strength of MAP also being reported with this rising behavior. Furthermore, the heights of the main peaks where C-S-H was present in the nBZs were higher than those in the BZs.

The NS preparation provided more $[SiO_4]^{4-}$ complexes for the matrix of MAP when compared with the NH one. The repolycondensation of $[SiO_4]^{4-}$ and $[AlO_4]^{5-}$ in the OH^- environment created by the NS preparation was more intense than that by the NH one. The intense repolycondensation accommodated the MAP produced with NS, creating an advantageous hydration state under which the physicochemical property and strength of the MAP built up consistently.

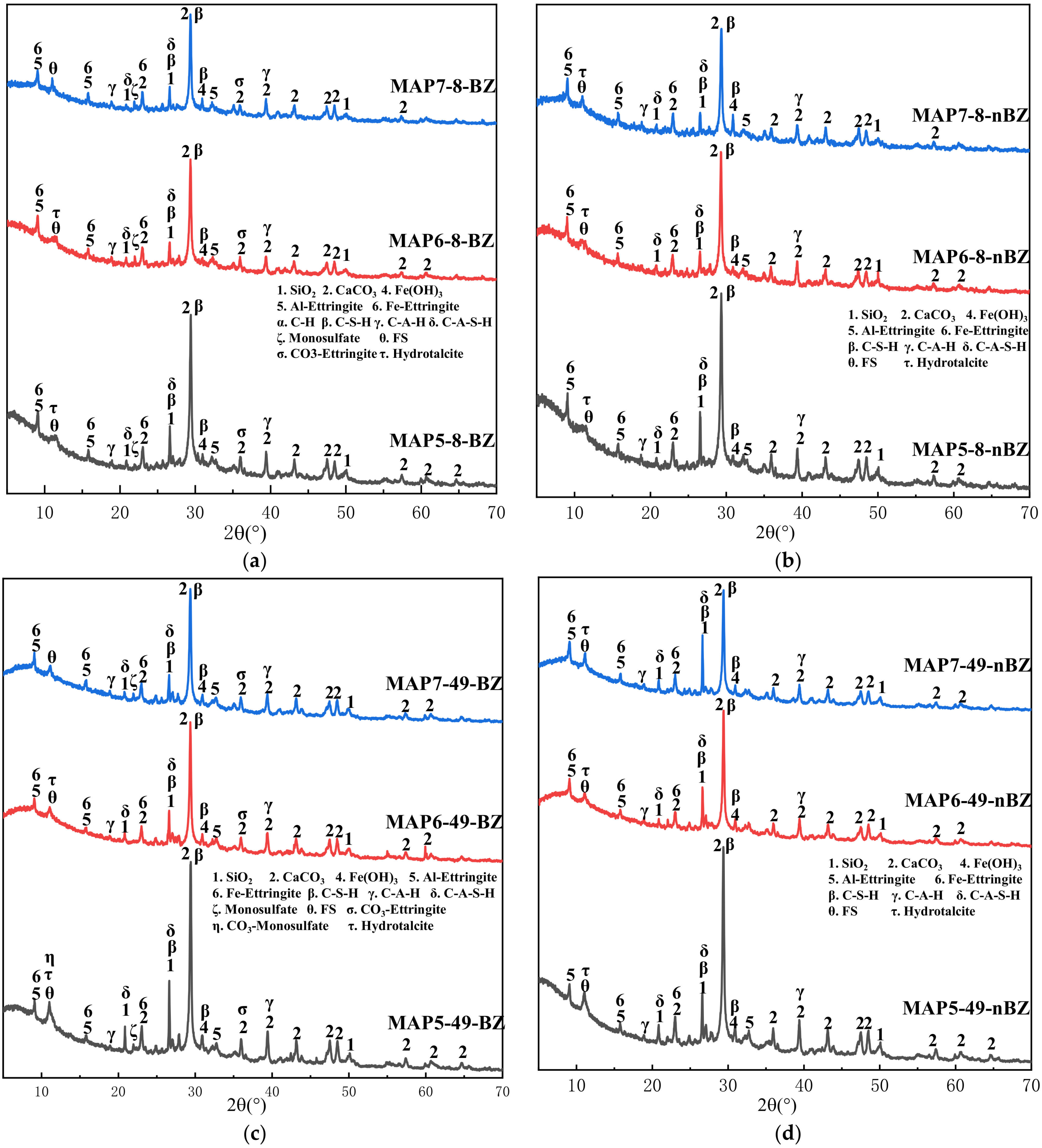

(**a**) (**b**)

(**c**) (**d**)

Figure 13. XRD patterns of NS as alkali agent. (**a**) XRD patterns at the BZ position for 8 days old; (**b**) XRD patterns at the nBZ position for 8 days old; (**c**) XRD patterns at the BZ position for 49 days old; (**d**) XRD patterns at the nBZ position for 49 days old.

3.2.4. SEM Results of MAP

1. SEM Analysis of MAP: NH as Alkali Agent

Figure 14 depicts the SEM images of the NH sub-specimens from BZs at 8 days old. The predominant hydrates in the NH sub-specimens from BZs at 8 days old included N-A-S-H, CH, C-S-H, C-A-H, C-A-S-H, monosulfate, FS, and $CaCO_3$.

Plentiful gel-like hydrates developed including CH, C-S-H, C-A-H, C-A-S-H, monosulfate, and FS in the NH sub-specimens produced with the mix ratio MAP4 at 8 days old, as shown in Figure 14(D1,D2). The gel-like hydrates established the consistent framework in MAP, the pores of which were also filled by FS, as shown in Figure 14(D2). Therefore, the NH sub-specimens produced with the mix ratio MAP4 at 8 days old achieved the compact microscopic structure that guaranteed higher UCTs that reached 8.3 MPa. By contrast, the main hydrate in the NH sub-specimens produced with the mix ratio MAP2 was the petal-like monosulfate that formed the widespread microscopic crevices in MAP, the maximal width of which reached 12.5 µm, as shown in Figure 15. Hence, the NH sub-specimens produced with the mix ratio MAP2 showed the loose framework which caused the MAP disintegration at 3 days old.

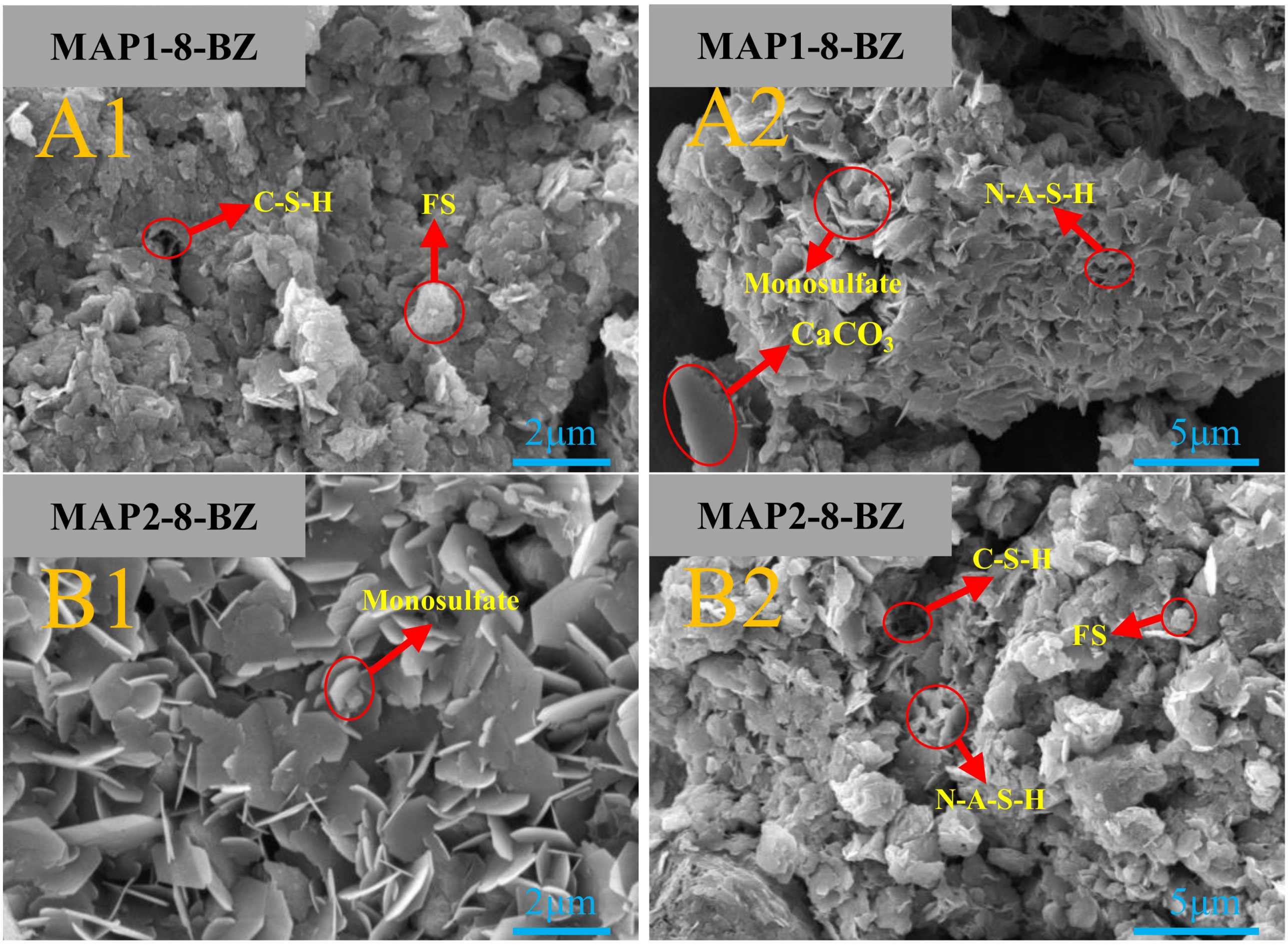

Figure 14. *Cont.*

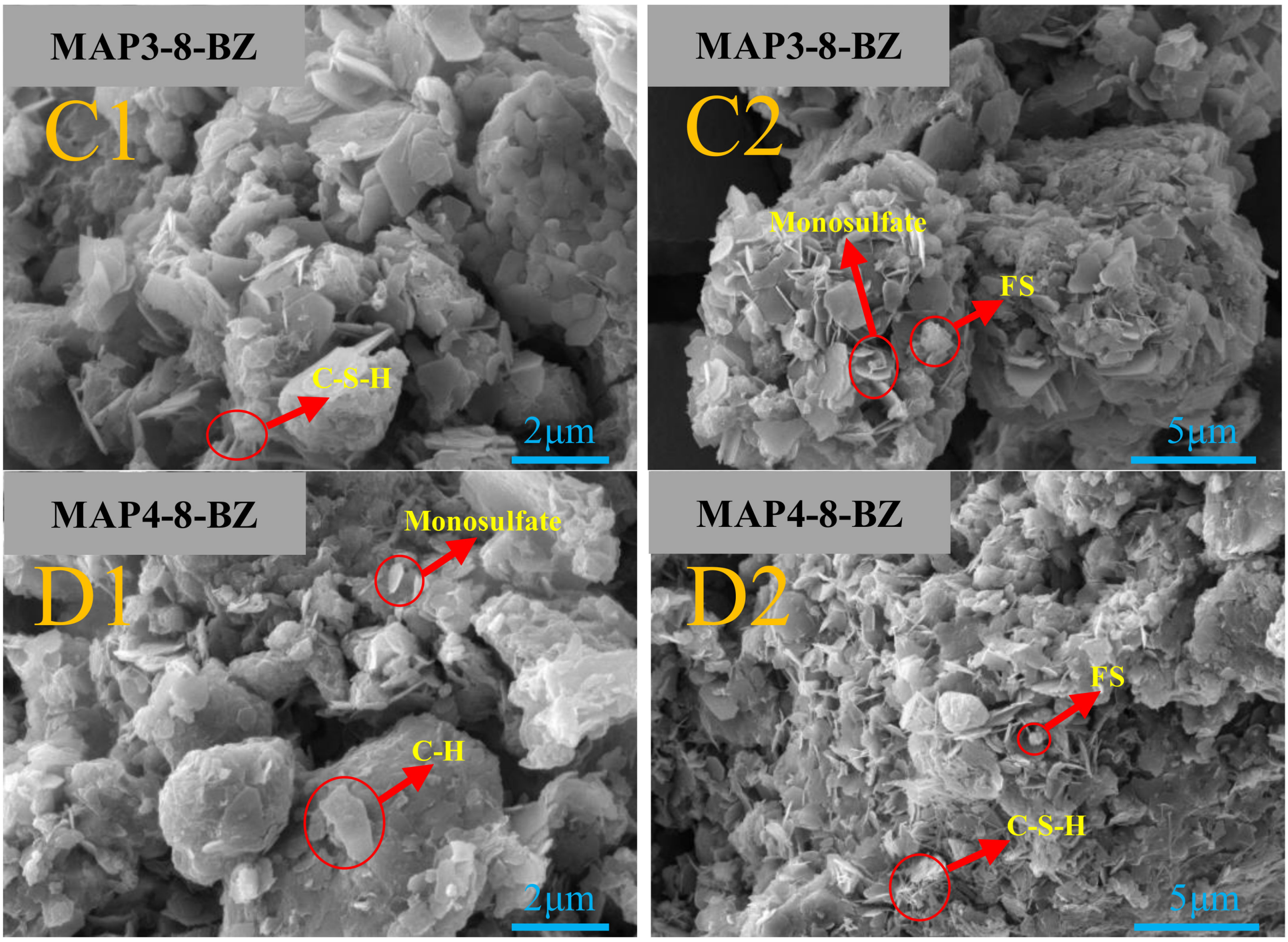

Figure 14. Microstructure of MAP1~4-8-BZ. (**A1**,**A2**) MAP1-8-BZ at 20 kx and 10 kx magnification; (**B1**,**B2**) MAP2-8-BZ at 20 kx and 10 kx magnification; (**C1**,**C2**) MAP3-8-BZ at 20 kx and 10 kx magnification; (**D1**,**D2**) MAP4-8-BZ at 20 kx and 10 kx magnification.

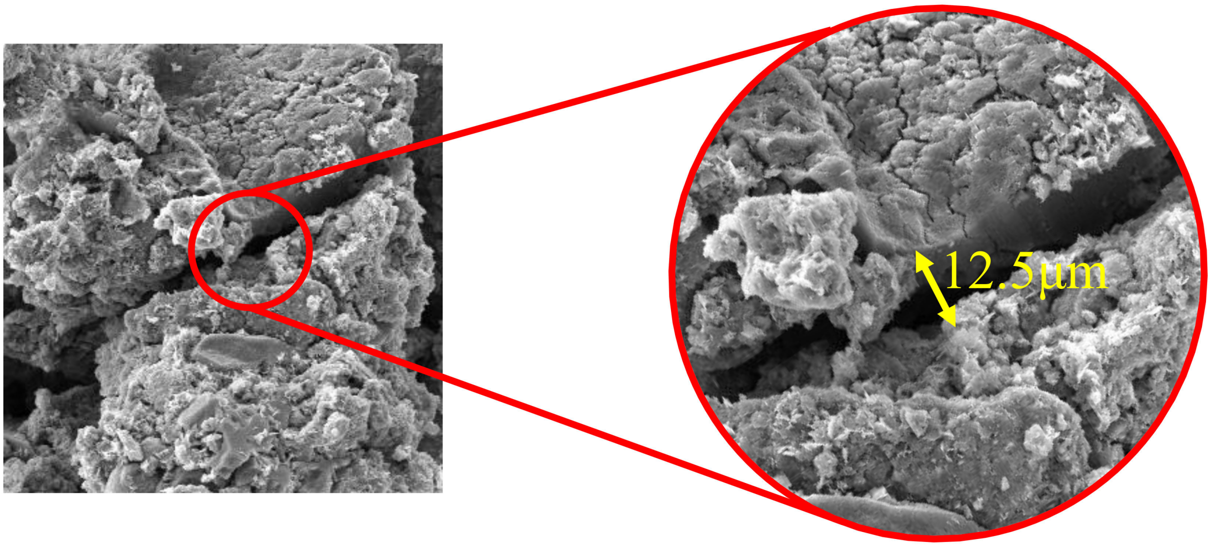

Figure 15. Cracks of MAP2-8-BZ.

Figure 16 depicts the SEM images of the NH sub-specimens from BZs at 49 days old. The predominant hydrates in the NH sub-specimens from BZs at 49 days old included N-A-S-H, CH, C-S-H, C-A-H, C-A-S-H, monosulfate, FS, $CaCO_3$, CO_3-Ettringite, and

SiO_2. The CO_3^{2-} complexes showed massive development in the grown MAP. CO_3^{2-} complex development also produced the tight combination with the matrix, as shown in Figure 16. The SEM image disclosed the ettringite in the nanopores that was not detected in XRD. The ettringite in the nanopores was covered by the thick gels of C-S-H and C-A-H, which helped produce the consistent framework in MAP. The consistent framework guaranteed the applicability of MAP in marine environments. Furthermore, the compactness of the microscopic structure in the grown MAP was constantly improved with hydrate development. In terms of the NH sub-specimens produced with the mix ratio P4, the size of the nanopores descended below 400 nm, as shown in Figure 17.

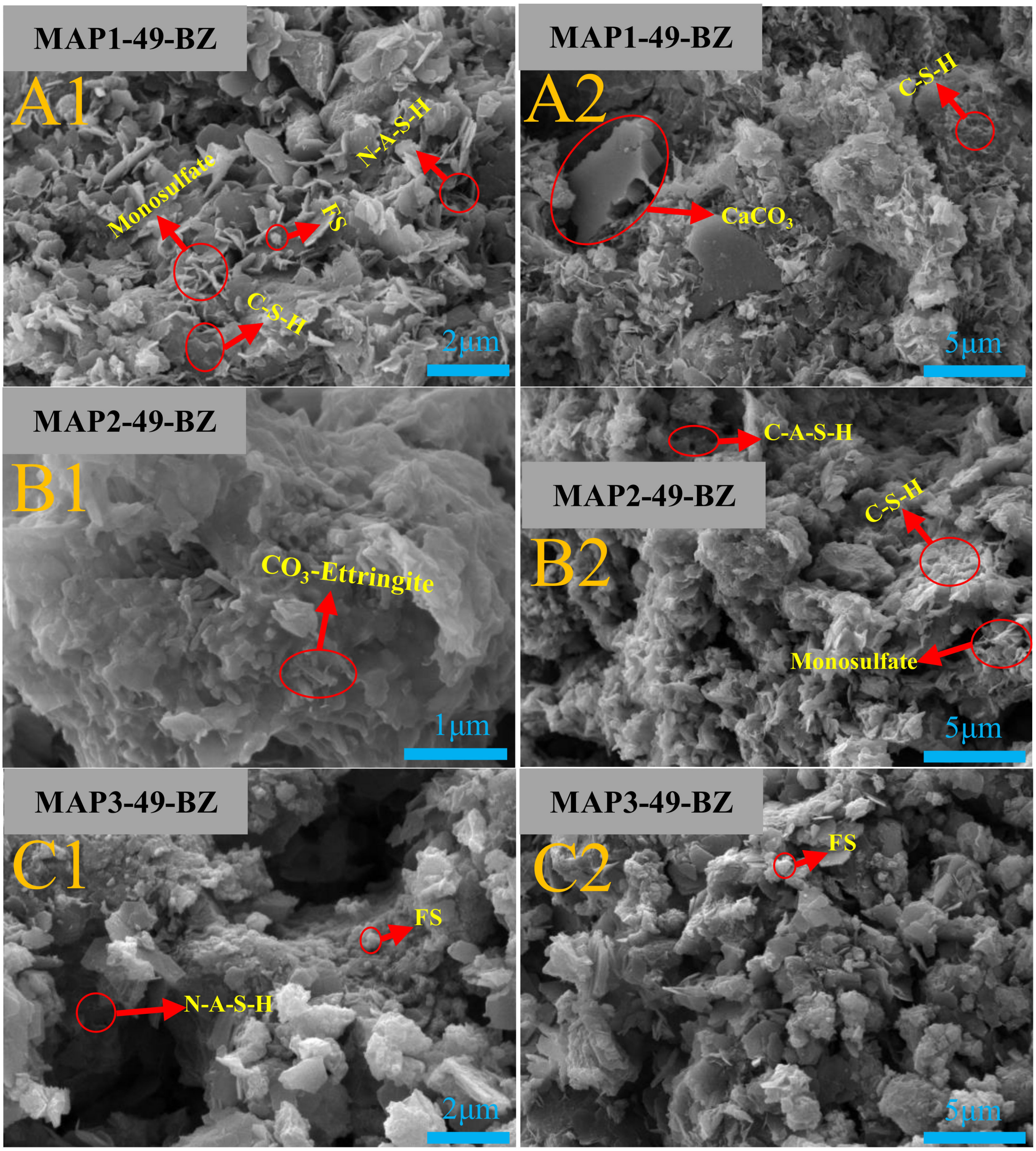

Figure 16. *Cont.*

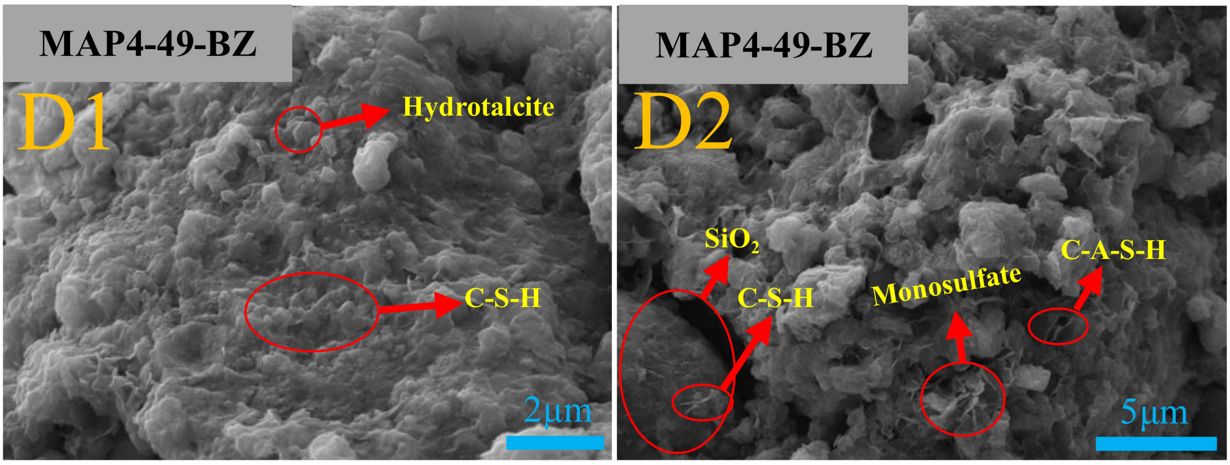

Figure 16. Microstructure of MAP1~4-49-BZ. (**A1**,**A2**) MAP1-49-BZ at 20 kx and 10 kx magnification; (**B1**,**B2**) MAP2-49-BZ at 20 kx and 10 kx magnification; (**C1**,**C2**) MAP3-49-BZ at 20 kx and 10 kx magnification; (**D1**,**D2**) MAP4-49-BZ at 20 kx and 10 kx magnification.

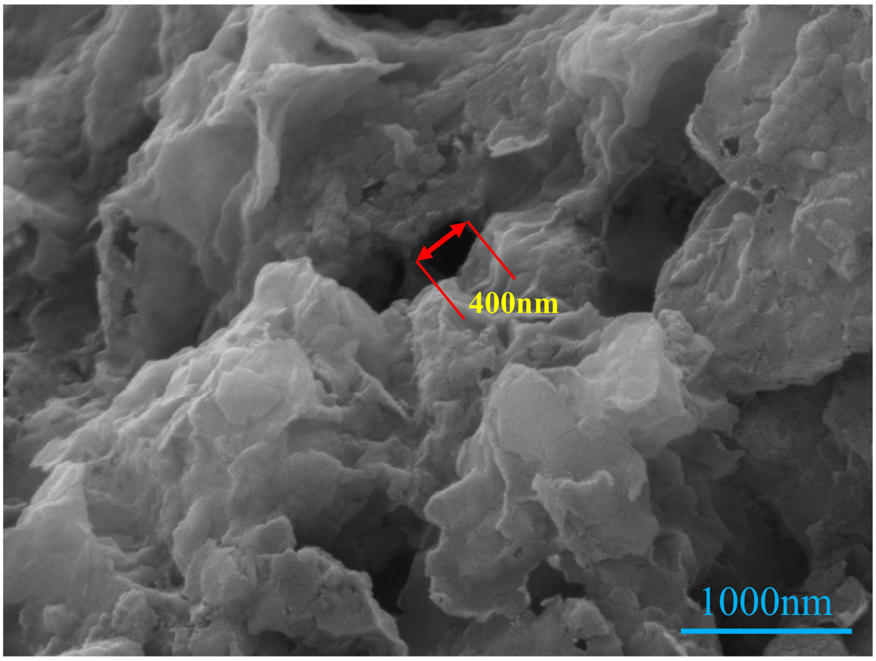

Figure 17. MAP4-49-BZ nanopore size micrograph.

2. SEM analysis of MAP: NS as alkali agent

Figure 18 depicts the SEM images of the NS sub-specimens from BZs at 8 days old. The predominant hydrates in the NS sub-specimens from BZs at 8 days old included C-S-H, C-A-S-H, ettringite, FS, and $CaCO_3$.

In terms of the NS sub-specimens from BZs at 8 days old, MAP5-8-BZ achieved the most consistent framework, in which the maximal diameter of the nanopore was below 500 nm, as shown in Figure 19. By contrast, the maximal width of the crevices in MAP6-8-BZ and MAP7-8-BZ was above 3 µm.

The nano-fibrous C-S-H and C-A-S-H gels were tightly combined, which formed the MAP5-8-BZ framework with the lattice pattern, as shown in Figure 18(A1). The development of C-S-H and C-A-S-H caused constant compaction for the MAP5-8-BZ framework during hydration at 8 days old when the reaction of $[SiO_4]^{4-}$, $[AlO_4]^{5-}$, and Ca^{2+} was intensified with the highest NS concentration. Meanwhile, the microscopic crevices were created around the nanopores filled by ettringite and bonded by the FS clusters, as shown in Figure 18(A1,A2). Therefore, the consistent framework composed of C-S-H, C-A-S-H, ettringite, and FS developed in P5-M1 and improved MAP UCTs that reached 8.3 MPa.

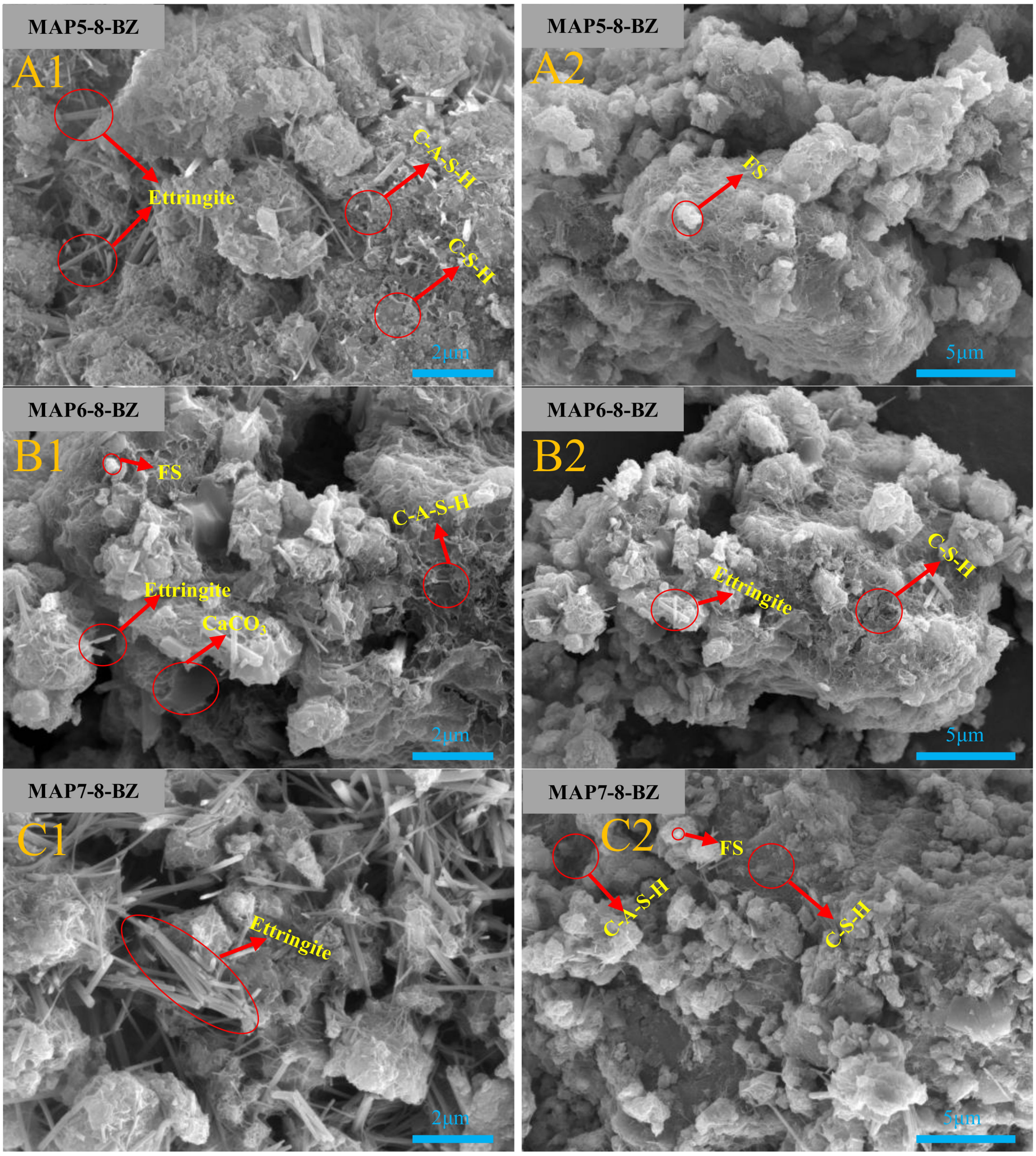

Figure 18. Microstructure of MAP5~7-8-BZ. (**A1**,**A2**) MAP5-8-BZ at 20 kx and 10 kx magnification; (**B1**,**B2**) MAP6-8-BZ at 20 kx and 10 kx magnification; (**C1**,**C2**) MAP7-8-BZ at 20 kx and 10 kx magnification.

The results from XRD reported the deficient development of C-S-H and C-A-S-H in MAP6-8-BZ and MAP7-8-BZ, the frameworks of which were looser than those of MAP5-8-BZ, as shown in Figure 18(B1–C2). The deficient development of C-S-H and C-A-S-H in MAP6-8-BZ and MAP7-8-BZ failed to tightly compress the MAP framework at 8 days old in which the ettringite grew freely in the open crevices. Hence, the diameter and length of ettringite in MAP7-8-BZ were 2 and 1.5 times those in MAP5-8-BZ, respectively. There were wider crevices left between the ettringite and the gels of C-S-H and C-A-S-H, the interfaces of which were not compactly bonded by the FS clusters. Meanwhile, the loose framework reserved more anions including OH^-, $[SiO_4]^{4-}$, and $[AlO_4]^{5-}$ than the consistent one. The grown MAP was then able to achieve more intense repolycondensation than the early-age one when the content of the anions reserved in the loose framework reached the proper level which accommodated the advantageous hydration state for the grown MAP. Therefore, there also was a close relation between the MAP framework and the NS concentration.

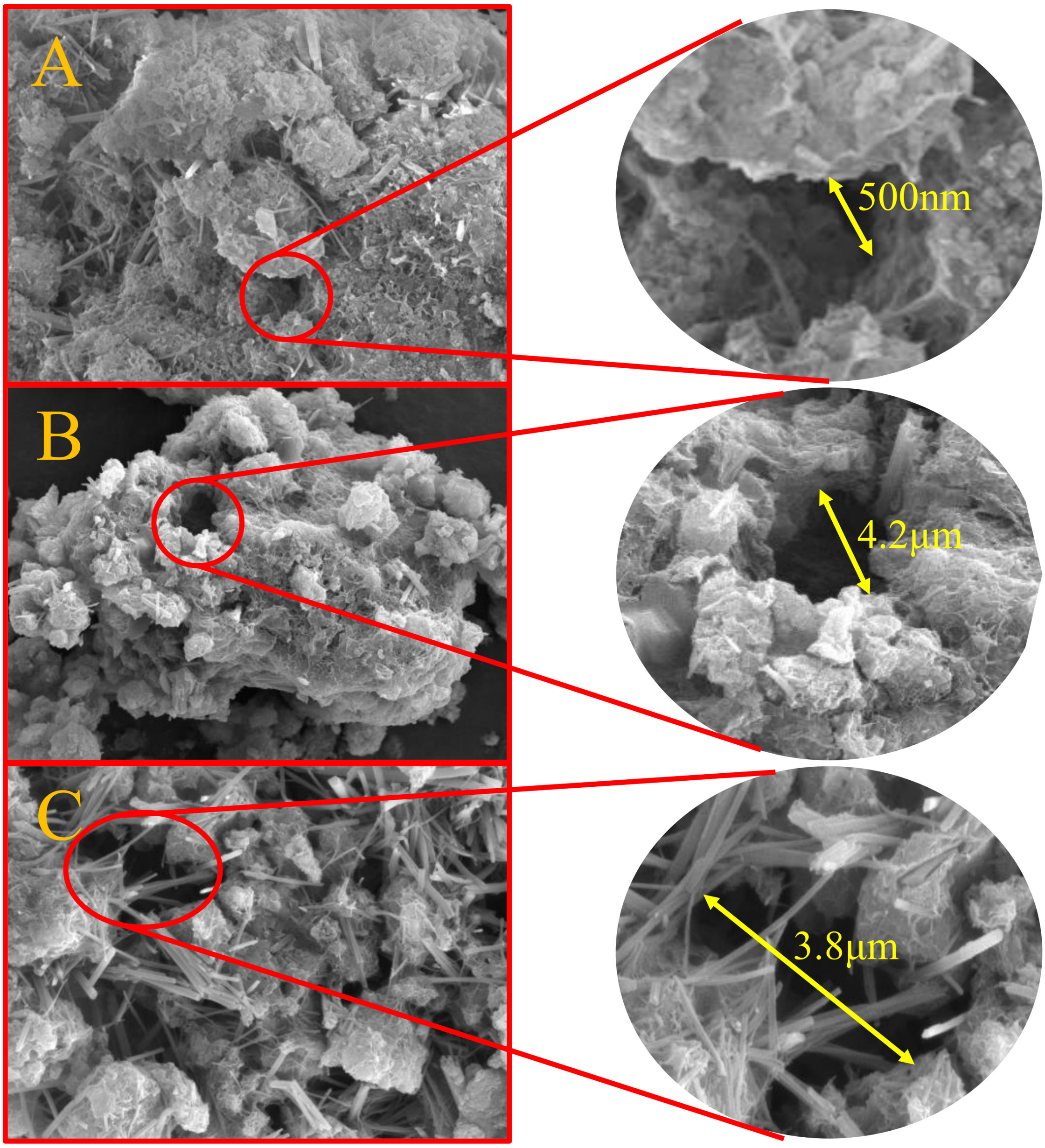

Figure 19. Pore size micrograph. (**A**) MAP5-8-BZ; (**B**) MAP6-8-BZ; (**C**) MAP7-8-BZ.

Figure 20 depicts the SEM images of the NS sub-specimens from BZs at 49 days old. The predominant hydrates in the NS sub-specimens from BZs at 49 days old included C-S-H, C-A-S-H, CO_3-Ettringite, ettringite, and FS. The age was also involved in the performance of MAP according to the SEM images from Figure 20. The grown MAP produced with a lower NS concentration received more of a supply of the anions including OH^-, $[SiO_4]^{4-}$, and $[AlO_4]^{5-}$ from the loose framework, which helped MAP7-49-BZ achieve more intense repolycondensation and realize more sufficient development of C-S-H and C-A-S-H at 49 days old than that with a higher NS concentration. Therefore, the element sizes of the lattice in the grown MAP produced with a lower NS concentration were finer than that with a higher NS concentration. The developed ettringite in MAP7-49-BZ played the role of fibers that reinforced the grown MAP produced with a lower NS concentration, which did not occur in MAP5-49-BZ due to the underdevelopment of ettringite in the early-age MAP.

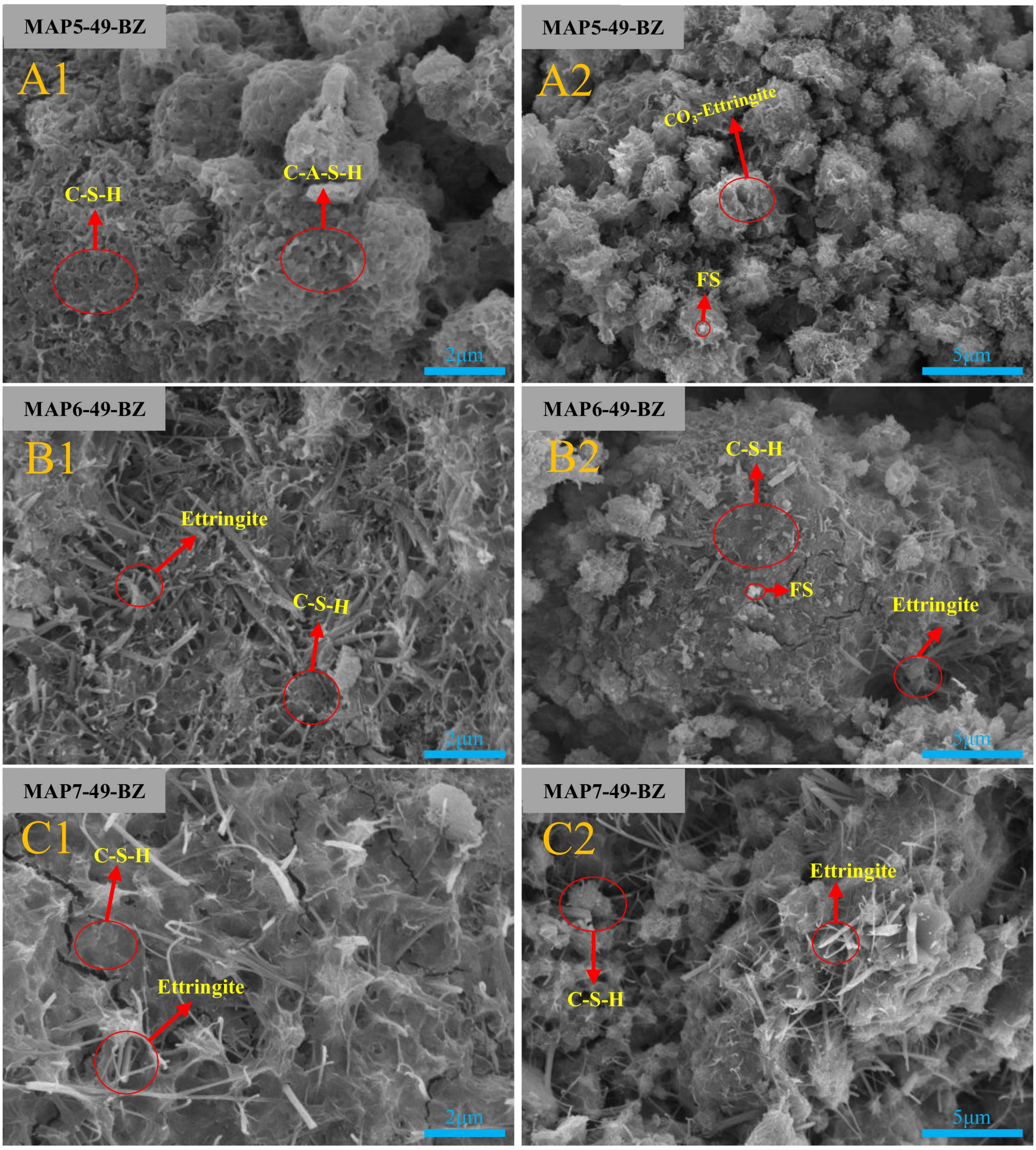

Figure 20. Microstructure of MAP5~7-49-BZ. (**A1**,**A2**) MAP5-49-BZ at 20 kx and 10 kx magnification; (**B1**,**B2**) MAP6-49-BZ at 20 kx and 10 kx magnification; (**C1**,**C2**) MAP7-49-BZ at 20 kx and 10 kx magnification.

The microscopic structure of MAP produced with NH showed the agglomeration feature. Particularly, the element sizes of the agglomeration in the early-age MAP produced with NH presented a certain difference which was diminished in the grown one. Therefore, NH preparation created the admirable porosity in MAP that could be improved by the proper NH concentration. Age accumulation certainly caused the diminishment of the MAP porosity in the marine environment. The results from XRD and SEM indicated that the MAP produced with NH generated more CO_3^{2-} complexes than that with NS. The CO_3^{2-} complexes were the main components of the agglomeration in the MAP produced with NH. Hence, carbonization also contributed to MAP porosity in the marine environment.

The microscopic structure of MAP produced with NS reported the lattice feature. Especially, the size of the elements in the grown MAP was finer than that in in the early-age one. Hence, the NS preparation created the excellent consistency in MAP that could be improved by the proper NS concentration. Age accumulation also raised the MAP consistency in the marine environment. Hence, the NH and NS preparation developed in this study created the promising physicochemical property and strength for NCBM application in the marine environment.

4. Conclusions

This study successfully developed MAP using SW, RPPs, and alkali agents such as NH and NS. The physicochemical properties and mechanical performance of MAP were comprehensively evaluated, yielding the following key conclusions:

1. The bistage crushing process significantly enhanced the physical reactivity of RPPs by increasing their specific surface area, which improved the material's reactivity during subsequent alkali activation and facilitated the formation of further hydration products in MAP.
2. The main hydration products in MAP were identified as C-S-H, C-A-S-H, N-A-S-H, FS, monosulfate, and $CaCO_3$. These products, particularly the N-A-S-H gel, contributed to the structural integrity of MAP and improved resistance to corrosive ions such as SO_4^{2-} and Cl^-, especially in NS-activated systems.
3. The compressive strength of MAP varied with the increase in curing age. This study found that MAP prepared with NS exhibited higher early-age strength, achieving a maximum of 8.3 MPa at 8 days compared to MAP prepared with NH, which reached a maximum of 5.59 MPa at the same age. By 49 days, MAP prepared with NS continued to show superior strength, with values ranging from 5.46 MPa to 7.34 MPa, whereas MAP prepared with NH exhibited a range from 3.59 MPa to 5.83 MPa. Additionally, certain MAP formulations showed strength gains with extended curing time, indicating that proper mix ratios can further enhance the mechanical properties of the material.
4. This study analysis revealed that MAP prepared with NS exhibited a more consistent and compact microstructure, characterized by well-formed C-S-H and C-A-S-H gels, which resulted in reduced porosity. In contrast, NH-prepared MAP displayed a more agglomerated structure, with CO_3^{2-} complexes contributing to the porosity. However, the gradual carbonation of these materials enhanced their compactness and strength over time in marine environments.
5. The MAP formulations demonstrated excellent adaptability to marine conditions. The development of N-A-S-H, FS, and reduced ettringite formation played a key role in preventing sulfate and chloride ion intrusion, ensuring the durability of MAP. These findings highlight the potential of MAP as a sustainable alternative for construction in marine and coastal environments.
6. This study developed an innovative MAP using SW, RPPs, and alkali agents, evaluated for its adaptability in marine conditions. Laboratory-scale testing limits the current findings. MAP long-term durability and performance in diverse harsh environments remain to be validated. Future work will optimize MAP mix designs for varied marine exposure levels, conduct field tests in marine structures, and explore applications in other harsh environments.
7. This study primarily relied on SEM imaging, which provides only 2D slice images of the material cross-section. This lack of 3D structural information may lead to biased interpretations of MAP's internal meso-structure, potentially affecting our understanding of pore distribution, crack networks, and the spatial arrangement of hydration products. Consequently, the relationship between mechanical performance and internal structure could be impacted. Future research would benefit from non-destructive 3D imaging techniques, such as CT scanning, to obtain accurate insights into MAP's true 3D morphology and distribution. As highlighted by Huang [33], 3D CT imaging

enables a deeper understanding of material meso-structures and allows for more precise correlations between mechanical performance and structural characteristics.

Author Contributions: Conceptualization, Y.B. and Y.W.; methodology, Y.B. and Y.W.; validation, Y.B., Y.W. and X.C.; formal analysis, Y.B.; investigation, Y.B.; resources, Y.B. and T.Y.; data curation, Y.B.; writing—original draft preparation, Y.B.; writing—review and editing, Y.B and Y.W.; visualization, Y.B.; supervision, Y.W.; project administration, Y.W. All authors have read and agreed to the published version of the manuscript.

Funding: This research received no external funding.

Data Availability Statement: The original contributions presented in this study are included in the article. Further inquiries can be directed to the corresponding author.

Acknowledgments: The authors thank all the people who have supported this research.

Conflicts of Interest: The authors declare no conflicts of interest.

Nomenclature

Al-Ettringite	$Ca_6Al_2(SO_4)_3(OH)_{12}\cdot 26H_2O$
CCBMs	conventional cement-based materials
CH	$Ca(OH)_2$
C_3S	$3CaO\cdot SiO_2$
C_2S	$2CaO\cdot SiO_2$
C_4AF	$4CaO\cdot Al_2O_3\cdot Fe_2O_3$
C_3A	$3CaO\cdot Al_2O_3$
C-S-H	$x CaO\cdot SiO_2\cdot n H_2O$
C-A-H	$x CaO\cdot Al_2O_3\cdot n H_2O$
C-A-S-H	$CaO\cdot Al_2O_3\cdot 2SiO_2\cdot 4H_2O$
C_4AH_{13}	$4CaO\cdot Al_2O_3\cdot 13H_2O$
CO_3-Ettringite	$3CaO\cdot Al_2O_3\cdot CaCO_3\cdot 32H_2O$
CC	critical concentration
EDS	Energy-Dispersive Spectrometer
FW	freshwater
FS	Friedel's salt
Fe-Ettringite	$Ca_3(Al_{0.8}Fe_{0.2})\cdot 3CaSO_4\cdot 32H_2O$
Hydrotalcite	$Mg_6Al_2CO_3(OH)_{16}\cdot 4H_2O$
MAP	marine alkali paste
Monosulfate	$3CaO\cdot Al_2O_3\cdot CaSO_4\cdot 12H_2O$
NCBMs	novel conventional cement-based materials
N-A-S-H	$Na_2O\cdot Al_2O_3\cdot xSiO_2\cdot 2H_2O$
OPC	ordinary Portland cement
PSs	parental specimens
RH	relative humidity
RPPs	recyclable particle material from paste specimens
RCW	reused construction waste
SW	seawater
SEM	thermal-field emission scanning electron microscopy
UCTs	uniaxial compression tests
XRD	X-ray diffraction

References

1. United Nations. Available online: https://www.un.org/development/desa/en/news/population/2018-revision-of-world-urbanization-prospects.html (accessed on 22 October 2024).
2. Zhang, M.; Li, W.; Wang, Z.; Liu, H. Urbanization and production: Heterogeneous effects on construction and demolition waste. *Habitat Int.* **2023**, *134*, 102778. [CrossRef]
3. Bao, Z. Developing circularity of construction waste for a sustainable built environment in emerging economies: New insights from China. *Dev. Built Environ.* **2023**, *13*, 100107. [CrossRef]

4. Zhao, Y.; Wang, T.; Yi, W. Emergy-accounting-based comparison of carbon emissions of solid waste recycled concrete. *Constr. Build. Mater.* **2023**, *387*, 131674. [CrossRef]
5. Amran, M.; Makul, N.; Fediuk, R.; Lee, Y.H.; Vatin, N.I.; Lee, Y.Y.; Mohammed, K. Global carbon recoverability experiences from the cement industry. *Case Stud. Constr. Mater.* **2022**, *17*, e01439. [CrossRef]
6. Belaïd, F. How does concrete and cement industry transformation contribute to mitigating climate change challenges? *Resour. Conserv. Recycl. Adv.* **2022**, *15*, 200084. [CrossRef]
7. Florea, M.V.A.; Ning, Z.; Brouwers, H.J.H. Activation of liberated concrete fines and their application in mortars. *Constr. Build. Mater.* **2014**, *50*, 1–12. [CrossRef]
8. He, Z.; Hu, R.; Ma, Z.; Liu, X.; Wang, C.; Wu, H. Reusing thermoactivated construction waste spoil as sustainable binder for durable concrete: Microstructure and chloride transport. *Constr. Build. Mater.* **2023**, *398*, 132553. [CrossRef]
9. Vashistha, P.; Oinam, Y.; Kim, H.-K.; Pyo, S. Effect of thermo-mechanical activation of waste concrete powder (WCP) on the characteristics of cement mixtures. *Constr. Build. Mater.* **2023**, *362*, 129713. [CrossRef]
10. Kravchenko, E.; Lazorenko, G.; Jiang, X.; Leng, Z. Alkali-activated materials made of construction and demolition waste as precursors: A review. *Sustain. Mater. Technol.* **2024**, *39*, e00829. [CrossRef]
11. Gu, F.; Xie, J.; Vuye, C.; Wu, Y.; Zhang, J. Synthesis of geopolymer using alkaline activation of building-related construction and demolition wastes. *J. Clean. Prod.* **2023**, *420*, 138335. [CrossRef]
12. Duan, Z.H.; Singh, A.; Xiao, J.Z.; Hou, S.D. Combined use of recycled powder and recycled coarse aggregate derived from construction and demolition waste in self-compacting concrete. *Constr. Build. Mater* **2020**, *254*, 119323. [CrossRef]
13. Lu, J.X.; Zhan, B.J.; Duan, Z.H.; Poon, C.S. Using glass powder to improve the durability of architectural mortar prepared with glass aggregates. *Mater. Des.* **2017**, *135*, 102–111. [CrossRef]
14. Sajedi, F.; Razak, H.A. Effects of thermal and mechanical activation methods on compressive strength of ordinary Portland cement–slag mortar. *Mater. Des.* **2011**, *32*, 984–995. [CrossRef]
15. Roy, D.M. Alkali-activated cements Opportunities and challenges. *Cem. Concr. Res.* **1999**, *29*, 249–254. [CrossRef]
16. Zhang, D.S.; Zhang, S.X.; Huang, B.W.; Yang, Q.N.; Li, J.B. Comparison of mechanical, chemical, and thermal activation methods on the utilisation of recycled concrete powder from construction and demolition waste. *J. Build. Eng.* **2022**, *61*, 105295. [CrossRef]
17. Sajedi, F.; Razak, H.A. Comparison of different methods for activation of ordinary Portland cement-slag mortars. *Constr. Build. Mater.* **2011**, *25*, 30–38. [CrossRef]
18. United Nations. Available online: https://www.unwater.org/publications/world-water-development-report-2018 (accessed on 22 October 2024).
19. Miller, S.A.; Horvath, A.; Monteiro, P.J.M. Impacts of booming concrete production on water resources worldwide. *Nat. Sustain.* **2018**, *1*, 69–76. [CrossRef]
20. Saxena, S.; Baghban, M.H. Seawater concrete: A critical review and future prospects. *Dev. Built Environ.* **2023**, *16*, 100257. [CrossRef]
21. Otsuki, N.; Saito, T.; Tadokoro, Y. Possibility of Sea Water as Mixing Water in Concrete. *J. Civ. Eng. Arch.* **2012**, *6*, 1273–1279. [CrossRef]
22. Sheng, Z.G.; Wang, Y.J.; Huang, D. A Promising Mortar Produced with Seawater and Sea Sand. *Materials* **2022**, *15*, 6123. [CrossRef]
23. Shi, D.; Yao, Y.; Ye, J.Y.; Zhang, W.S. Effects of seawater on mechanical properties, mineralogy and microstructure of calcium silicate slag-based alkali-activated materials. *Constr. Build. Mater.* **2019**, *212*, 569–577. [CrossRef]
24. *GB/T 1346-2011*; Test Methods for Water Requirement of Normal Consistency, Setting Time, and Soundness of Portland Cement. Standardization Administration of China: Beijing, China, 2011.
25. *GB/T 17671-2021*; Test Method of Cement Mortar Strength (ISO Method). Standardization Administration of China: Beijing, China, 2021.
26. Ohemeng, E.A.; Ekolu, S.O. A review on the reactivation of hardened cement paste and treatment of recycled aggregates. *Mag. Concr. Res.* **2020**, *72*, 526–539. [CrossRef]
27. Bannister, F.A.; Hey, M.H.; Bernal, J.D. Ettringite from Scawt Hill, Co. Antrim. *Mineral. Mag.* **1936**, *24*, 324–329. [CrossRef]
28. Moore, A.E.; Taylor, H.F.W. Crystal Structure of Ettringite. *Nature* **1968**, *218*, 1048–1049. [CrossRef]
29. Hartman, M.R.; Berliner, R. Investigation of the structure of ettringite by time-of-flight neutron powder diffraction techniques. *Cem. Concr. Res.* **2006**, *36*, 364–370. [CrossRef]
30. Lee, N.K.; Lee, H.K. Influence of the slag content on the chloride and sulfuric acid resistances of alkali-activated fly ash/slag paste. *Cem. Concr. Compos.* **2016**, *72*, 168–179. [CrossRef]
31. Ismail, I.; Bernal, S.A.; Provis, J.L.; San Nicolas, R.; Brice, D.G.; Kilcullen, A.R.; Hamdan, S.; van Deventer, J.S.J. Influence of fly ash on the water and chloride permeability of alkali-activated slag mortars and concretes. *Constr. Build. Mater.* **2013**, *48*, 1187–1201. [CrossRef]
32. Siddique, S.; Jang, J.G. Acid and sulfate resistance of seawater based alkali activated fly ash: A sustainable and durable approach. *Constr. Build. Mater.* **2021**, *281*, 122601. [CrossRef]
33. Huang, Y.; Yang, Z.; Ren, W.; Liu, G.; Zhang, C. 3D meso-scale fracture modelling and validation of concrete based on in-situ X-ray Computed Tomography images using damage plasticity model. *Int. J. Solids Struct.* **2015**, *67–68*, 340–352. [CrossRef]